Storage and Evolution of Mafic and Intermediate Alkaline Magmas beneath Ross Island, Antarctica

Kayla Iacovino[1]*, Clive Oppenheimer[1], Bruno Scaillet[2] and Philip Kyle[3]

[1]Department of Geography, University of Cambridge, Cambridge CB2 3EN, UK; [2]Institut des Sciences de la Terre d'Orléans, Université d'Orléans–CNRS–BRGM, 45071 Orléans Cedex 2, France and [3]Department of Earth and Environmental Science, New Mexico Institute of Mining and Technology, Socorro, NM 87801, USA

*Corresponding author. Present address: US Geological Survey, Mail Stop 910, 345 Middlefield Road, Menlo Park, CA 94025, USA. Telephone: +1 (650) 329-4986. E-mail: kiacovino@usgs.gov

ABSTRACT

We present the results of phase equilibrium experiments carried out on basanite and phonotephrite lavas from Ross Island, Antarctica. Experiments were designed to reproduce the P–T–X–fO$_2$ conditions of deep and intermediate magma storage and to place constraints on the differentiation of each of the two predominant lava suites on the island, which are thought to be derived from a common parent melt. The Erebus Lineage (EL) consists of lava erupted from the Erebus summit and the Dry Valley Drilling Project (DVDP) lineage is represented by lavas sampled by drill core on Hut Point Peninsula. Experiments were performed in internally heated pressure vessels over a range of temperatures (1000–1150°C) and pressures (200–400 MPa), under oxidized conditions (NNO to NNO + 3, where NNO is the nickel–nickel oxide buffer), with X_{H_2O} of the H$_2$O–CO$_2$ mixture added to the experimental capsule varying between zero and unity. The overall mineralogy and mineral compositions of the natural lavas were reproduced, suggesting oxidizing conditions for the deep magma plumbing system, in marked contrast to the reducing conditions (QFM to QFM – 1, where QFM is the quartz–fayalite–magnetite buffer) in the Erebus lava lake. In basanite, crystallization of spinel is followed by olivine and clinopyroxene; olivine is replaced by kaersutitic amphibole below ~1050°C at intermediate water contents. In phonotephrite, the liquidus phase is kaersutite except in runs with low water content (XH$_2$O^{fluid} < 0·2) where it is replaced by clinopyroxene. Experimental kaersutite compositions suggest that the amphibole-bearing DVDP lavas differentiated below 1050°C at 200–400 MPa and NNO + 1·5 to NNO + 2. Olivine- and clinopyroxene-bearing EL lavas are consistent with experiments performed above 1050°C and pressures around 200 MPa. The plagioclase liquidus at <1–2 wt % H$_2$O suggests extremely dry conditions for both lineages (XH$_2$O^{fluid} approaching zero for EL, ~0·25 for DVDP), probably facilitated by dehydration induced by a CO$_2$-rich fluid phase. Our results agree with previous studies that suggest a single plumbing system beneath Ross Island in which DVDP lavas (and probably other peripheral volcanic products) were erupted through radial fractures associated with the ascent of parental magma into the lower crust. The longer travel time of the DVDP lavas through the crust owing to lateral movement along fractures and the lack of a direct, sustained connection to the continuous CO$_2$-rich gas flux that characterizes the main central Erebus conduit is probably responsible for the lower temperatures and slightly wetter conditions and hence the change in mineralogy observed.

Key words: alkaline volcanism; basanite; CO$_2$; phase equilibria; phonotephrite; Ross Island

INTRODUCTION

Ross Island, Antarctica (77°32'S, 167°10'E) is part of the Erebus Volcanic Province (EVP) and comprises five predominant volcanic centers. The currently active and volumetrically dominant Erebus volcano is surrounded by the now extinct subsidiary volcanic centers of Mts Bird, Terror, Terra Nova, and Hut Point Peninsula (Fig. 1). Erebus is known for its persistently active phonolitic lava lake, which has been at the focus of recent active monitoring and petrological studies as it represents a window into the shallow regions of the alkaline intraplate volcanic plumbing system. Recent investigations employing experimental petrological work (Moussallam *et al.*, 2013) and seismic tomography (Zandomeneghi *et al.*, 2013) have placed tight constraints on the physical and petrological properties of the shallow plumbing system and phonolitic lava lake including its geometry, temperature, pressure, and oxygen fugacity. These studies have the potential to refine the results of numerical models developed for the shallow Erebus system, such as those of Burgisser *et al.* (2012) and Molina *et al.* (2012). The intermediate and deep plumbing system beneath Erebus (>8 km depth) has been investigated via study of a suite of melt inclusions (Oppenheimer *et al.*, 2011) and mixed volatile solubility experiments (Iacovino *et al.*, 2013), which have placed constraints on the depths of degassing and the equilibrium fluid contents of primitive and intermediate composition magmas. Little is known, however, about the specific P–T–X–fO_2 conditions of magma storage and differentiation processes at these depths. Understanding the deep system at Erebus is crucial because the constant supply of deeply derived CO_2-rich gases combined with a sustained energy and mass input into the lava lake suggests a direct link between the phonolitic lava lake and the mantle source of the parental magmas via a deep mafic plumbing system (Kyle *et al.*, 1992; Oppenheimer & Kyle, 2008; Oppenheimer *et al.*, 2011).

Gas emissions from the Erebus lava lake are rich in CO_2 ($\sim$30 mol %) and comparatively low in H_2O ($\sim$65 mol %; Oppenheimer *et al.*, 2011; Burgisser *et al.*, 2012), consistent with the volatile compositions deduced from melt inclusions for the deeper system. The longevity of the lava lake itself is hypothesized to reflect, in part, the constant fluxing of heat and CO_2-rich fluid (Oppenheimer *et al.*, 2011) that originates from depths greater than those recorded by the most primitive melt inclusions (Iacovino *et al.*, 2013*a*). Indeed, many separate studies have concluded that various aspects of the Erebus system are controlled by the influx of heat and CO_2, including polybaric fractional crystallization throughout the magmatic system (Oppenheimer *et al.*, 2011), the bimodal eruptive behavior in the lava lake (Oppenheimer & Kyle, 2008), shallow magma chamber processes (Moussallam *et al.*, 2013), and fumarolic degassing and the formation of ice caves and ice towers (Curtis & Kyle, 2011). CO_2 flushing has been invoked to explain the characteristics of degassing and melt inclusions at other volcanoes including Stromboli (Allard, 2010), Vesuvius
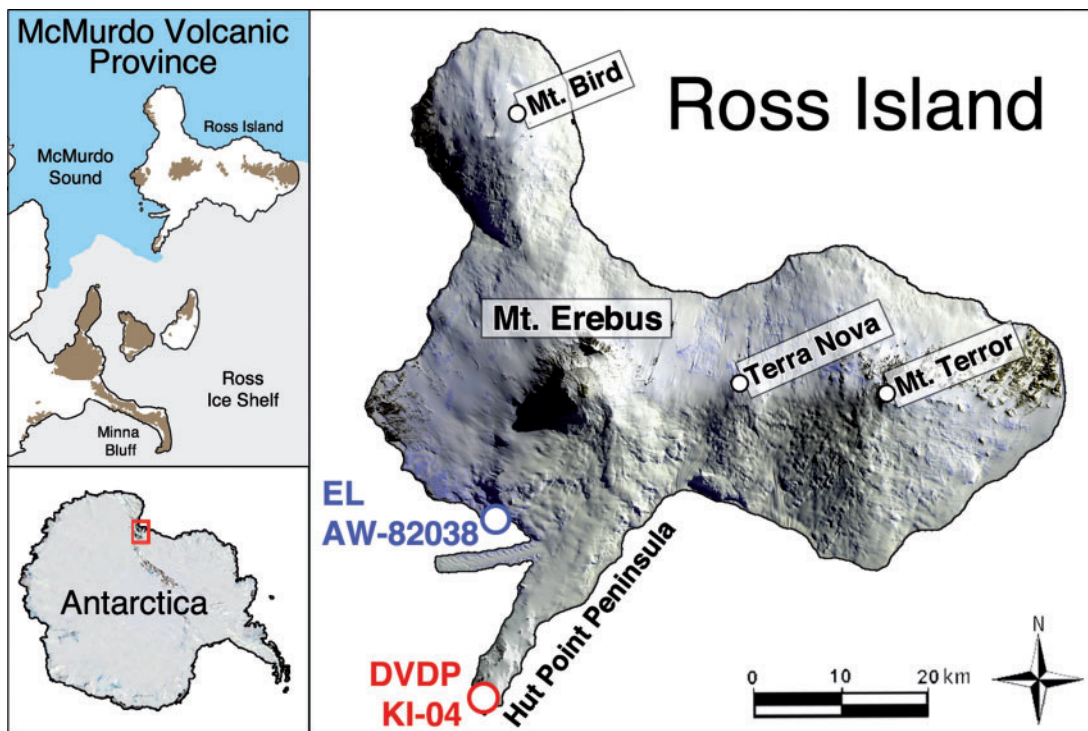
Fig. 1. Map showing the location of Ross Island within the McMurdo Volcanic Province, Antarctica. Erebus volcano is surrounded by the peripheral volcanic cones Bird, Terra Nova, Terror, and Hut Point Peninsula. The locations of the DVDP and EL samples collected for this experimental study are indicated.

(Marianelli *et al.*, 2005), Etna (Spilliaert *et al.*, 2006; Shinohara *et al.*, 2008; Tagliani *et al.*, 2012) and volcanoes in southeastern Guatemala (Walker *et al.*, 2003) that sit atop large sedimentary carbonate sequences, the devolatilization of which could provide the necessary excess carbon (Iacono-Marziano *et al.*, 2009). As Erebus has no such shallow carbon reservoir and probably derives all of its volatiles from the same mantle source responsible for magma production, we propose Erebus as the archetype for mantle-sourced carbon-controlled volcanism on Earth.

Subsidiary extinct volcanic centers and cones on Ross Island are distributed radially around Erebus at *c.* 120° from each other. This symmetrical distribution has been hypothesized to be the result of radial fractures created by the pressure of updoming mantle material on the crust directly beneath Mount Erebus (Kyle & Cole, 1974; Kyle *et al.*, 1992). The rare earth element patterns in primary Ross Island basanitoids indicate the generation of a basanitic parent magma through low-degree partial melting of the mantle source (Sun & Hanson, 1975, 1976). Major and trace element modeling suggests that lavas from Erebus [the Erebus Lineage (EL)] and the peripheral Hut Point Peninsula [the Dry Valley Drilling Project (DVDP) lineage] both evolved from a common basanite parent melt, which underwent two distinct fractional crystallization trends (Kyle, 1981; Kyle *et al.*, 1992). So far experimental work has focused on the evolved magmas (Moussallam *et al.*, 2013) and no experimental work is available to constrain storage and differentiation conditions of mafic lavas at Erebus (or other subsidiary volcanoes).

In this experimental study, one lava from each of the two Ross Island lava lineages (EL phonotephrite AW-82038 and DVDP basanite KI-04) were chosen as starting materials for equilibrium crystallization experiments to establish the $P–T–X–fO_2$ conditions necessary to produce the observed natural rock series. Phase equilibrium experiments are commonly used to constrain the pre-eruptive storage conditions of magmas, as well as their liquid line of descent (Sack *et al.*, 1987; Moore & Carmichael, 1998; Freise *et al.*, 2003; Martí *et al.*, 2008; Andújar *et al.*, 2010; Di Carlo *et al.*, 2010). Although non-equilibrium processes such as magma mixing and repeated replenishment of the system are important to consider, high pressure–temperature experimentation nevertheless illuminates the fundamental processes that control magma evolution from mantle to surface, allowing us to evaluate to what extent crystal–liquid equilibrium has been attained or maintained at depth.

Experiments were performed over a range of temperatures (1000–1150°C) and at pressures between 200 and 400 MPa to reproduce the intermediate region of the magma plumbing system where much early crystallization (differentiation of a basanitic parent to form intermediate lavas) is thought to occur. A temperature of 1000°C was chosen as a thermal lower bound, as the temperature of the surficial lava lake, which should be the coolest region of the plumbing system, has been constrained to ∼1000°C by several studies (Kyle, 1977; Caldwell & Kyle, 1994; Dunbar *et al.*, 1994). The resulting experimental charges thus span the entire range of compositions seen in the natural lavas, allowing elucidation of the evolutionary processes occurring throughout the Ross Island magmatic plumbing system. With this approach, our aim has been two-fold: (1) to experimentally establish the conditions necessary to derive the distinct Erebus and DVDP lineages from a hypothesized single basanite parent; (2) to place constraints on the intermediate Erebus and DVDP plumbing systems with respect to pressure, temperature, oxygen fugacity, and dominant volatiles (H_2O and CO_2).

Experiments with $H_2O–CO_2$ fluid compositions in the range of $XH_2O = 0–1$ not only help elucidate the role of H_2O in controlling phase equilibria, but also constrain the effect of CO_2 on crystallization processes via melt dehydration. Given that carbon dioxide is known to play an important role in the genesis of alkaline magmas, in both the mantle (Spera, 1984) and crust (Kaszuba & Wendlandt, 2000), it is important to understand its role at Erebus throughout the magmatic system (from mantle to surface).

Mineralogy and petrology of Ross Island lavas

The majority of lavas on Ross Island are represented by two strongly undersaturated sodic differentiation lineages: the Erebus Lineage (EL), made up of lavas erupted from Erebus volcano, and the Dry Valley Drilling Project (DVDP) lineage, made up of lavas on the Hut Point Peninsula and sampled via drill coring. The rarer Enriched-Iron Series (EFS) lavas are less silica-undersaturated and constitute only a small volume of Ross Island rocks. The EFS will not be discussed in this study. The DVDP and Erebus lineages are similar in terms of whole-rock chemistry as demonstrated by the similar variation in major element evolution of the DVDP and EL lavas with the exception of P_2O_5 (Fig. 2), the variation of which is probably being controlled by apatite crystallization. Major element mass balance and trace element modeling of DVDP and EL rocks (Kyle, 1981; Kyle *et al.*, 1992) suggests fractional crystallization from a common basanitic parent melt, with slight differences in differentiation conditions resulting in the two similar yet distinct lineages.

The mineralogy of the EL and DVDP lineage rocks from Ross Island has been extensively documented by Kyle *et al.* (1992) and Kyle (1981), respectively, whose observations are summarized below. These lineages share the same assemblage with two notable exceptions. First, kaersutitic amphibole is present in almost all DVDP lavas (except in basanites where it is rare) but is absent in EL lavas. Second, olivine is present in all EL lavas and in DVDP basanites, but occurs only as xenocrysts in more evolved DVDP lavas. In the EL rocks, olivine ranges in composition from Fo_{88} in basanites to Fo_{51} in phonolites. Olivine xenocrysts are rare and occur only in the most primitive lavas. In the DVDP
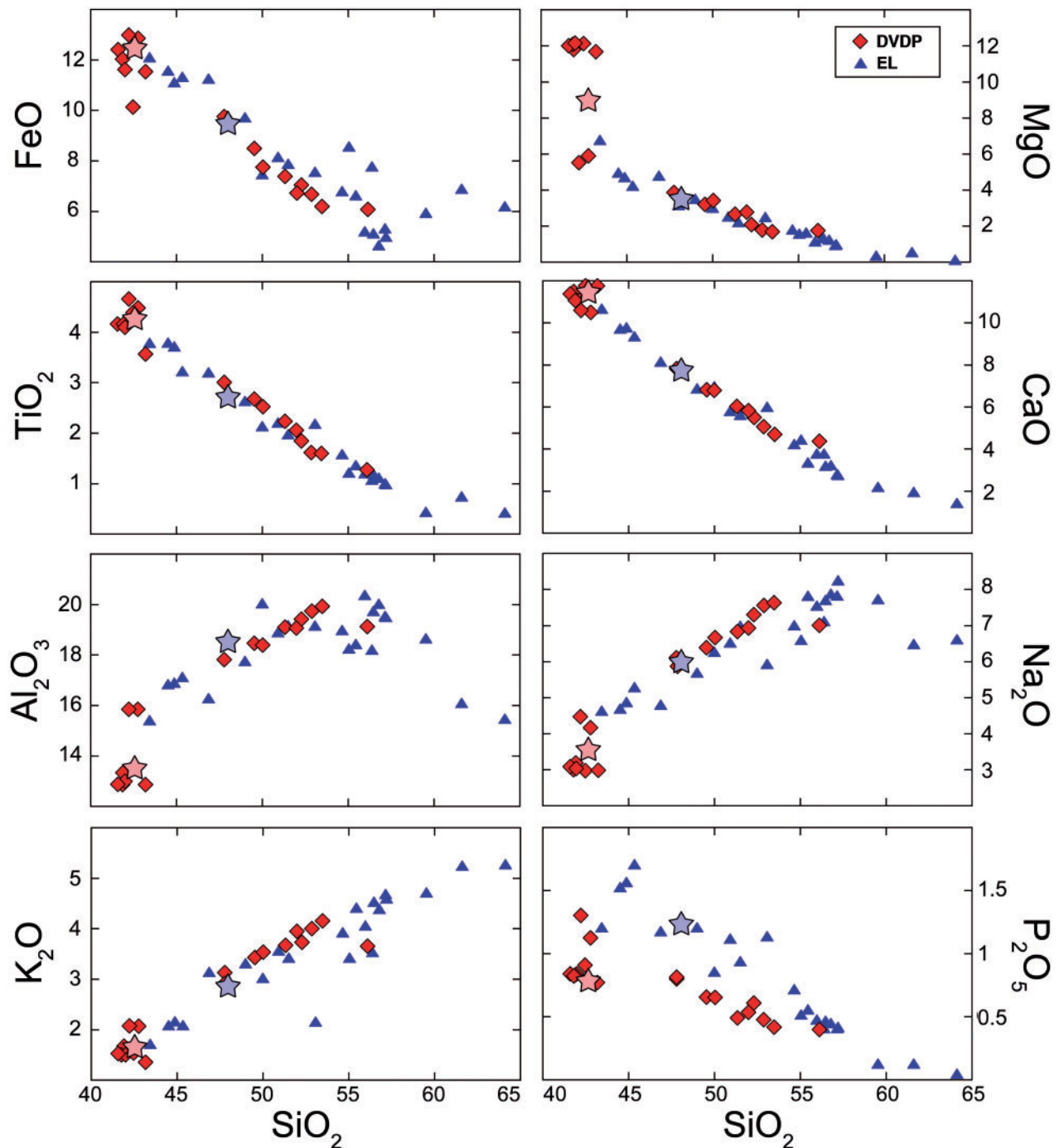
Fig. 2. Variation diagrams illustrating the evolution of the DVDP lineage (red diamonds; Kyle, 1981) and Erebus Lineage (EL; blue triangles; Kyle *et al.*, 1992). For whole-rock compositions the major element totals are normalized to 100%. One lava sample from each of these two lineages (red star: DVDP KI-04; blue star: EL AW-82038) was used as the starting material for the experimental work.

lavas, olivine occurs only in basanites as euhedral to subhedral phenocrysts and in the groundmass.

Clinopyroxene is ubiquitous in all EL and DVDP lavas and occurs as euhedral to subhedral phenocrysts. Pyroxenes with green cores, which show irregular rims, possibly owing to resorption, are occasionally found in DVDP lavas. In the EL lavas, clinopyroxenes show oscillatory zoning in basanites and intermediate lavas, but no zoning in phonolites.

Kaersutite is absent in EL lavas but is an important phase in all DVDP lavas except the basanites where it is rare. In some phonotephrites, kaersutite ranges from euhedral grains to those showing strong resorption and oxidation. It was suggested by Kyle (1981), based on previous experimental work, that temperature and PH_2O probably exert a strong control on the appearance or absence of kaersutite in DVDP and Erebus lineages, respectively.

Feldspar is the modally dominant phenocryst phase in EL lavas (up to 40% of the mode in anorthoclase-bearing phonolites) with compositions ranging from An_{72} to An_{59} in basanites, becoming increasingly albitic in the more evolved lavas. The feldspar in the EL phonolite is primarily anorthoclase. In the DVDP lava, feldspar occurs mostly as microphenocrysts or in the groundmass and is mainly labradorite (An_{50-60}) in basanites, and andesine to oligoclase in all other lava types.

Feldspathoids occur in the groundmass of the EL lavas, as nepheline, which contains up to 24% normative Ne. Microphenocrysts of apatite are common in most rocks of both lineages and are often found as inclusions in kaersutite and magnetite in the DVDP rocks. Pyrrhotite is present in all rocks from both lineages and occurs as small round blebs, suggesting the presence of an immiscible sulfide liquid in the Ross Island magmas. Opaque Fe–Ti oxides are common in both lava suites and are typically titanomagnetite as phenocrysts and in the groundmass, plus rare ilmenite phenocrysts.

EXPERIMENTAL METHODS

Starting materials

To investigate the evolution of the Ross Island magmas and the two dominant lava lineages, two samples were chosen, one from each lineage (Table 1): AW-82038 is an Erebus Lineage phonotephrite lava ($SiO_2 = 48.01$ wt %; $MgO = 3.18$ wt %) from Turk's Head (Kyle *et al.*, 1992) representative of intermediate EL lavas; KI-04 is a basanite ($SiO_2 = 43.06$ wt %; $MgO = 8.92$ wt %) collected from Hut Point Peninsula for this study and represents the less evolved magmas of the DVDP lineage. Figure 3 illustrates our starting material compositions relative to those of a suite of melt inclusions in Erebus Lineage rocks, which provides a representative cross-section through the evolutionary chemical trend of lavas on Ross Island (Oppenheimer *et al.*, 2011).

The AW-82038 phonotephrite [also referred to as Ne hawaiite by Kyle *et al.* (1992)] is weakly porphyritic (<8% phenocrysts) with a phenocryst assemblage of plagioclase, olivine, clinopyroxene, Fe–Ti oxides, apatite and rare accessory nepheline. AW-82038 is consistent with the fractionation of 12% olivine, 35% clinopyroxene, 7% Fe–Ti oxides, and 1% apatite from a basanitic parent, yielding a 43% residual melt (basanite DVDP 2-105.53; Kyle *et al.*, 1992).

In the KI-04 basanite, phenocrysts constitute around 12 vol. % and include olivine (6 vol. %), plagioclase feldspar (2 vol. %), augite (2 vol. %), apatite (1 vol. %), and titanomagnetite (<1 vol. %). Although kaersutitic amphibole is common in almost all DVDP lavas, it is rare in DVDP basanites and is absent in KI-04. Crystal distribution is relatively homogeneous throughout the sample. This sample is consistent with 17% fractionation from basanitic parent DVDP 2-105.53 yielding an 83% residual melt.

The lavas were crushed to a powder and melted in a Pt crucible in a 1 atm furnace at 1300°C. Sample AW-82038 was held in the furnace for ~30 min under a stream of nearly pure CO_2 (corresponding to an oxidation state near the Ni–NiO buffer, NNO) and then drop-quenched into cold water [sample prepared by Iacovino *et al.* (2013*a*)]. Sample KI-04 was held in furnace for ~1 h in air (i.e. extremely oxidizing conditions) and then removed from the furnace and immediately placed into cold water to quench. The resulting glassy samples were extracted from their crucibles, re-crushed, and re-melted under identical conditions to ensure a homogeneous and crystal-free glass. A portion of each starting material was polished and analyzed by electron microprobe to verify that no compositional changes had occurred during melting (see Table 1).

Experimental techniques

Between 30 and 60 mg of glassy starting material powder was added to $Au_{80}Pd_{20}$ capsules with lengths of ~20 mm, an outer diameter of 2.9 mm, and an inner diameter of 2.5 mm. Liquid H_2O was added via a microsyringe (~0–6 mg), and CO_2 was added as silver oxalate powder ($Ag_2C_2O_4$, ~0–18 mg). The X_{H2O} in the H_2O–CO_2 mixture of pre-run charges was varied at steps between zero and unity (i.e. $X_{H2O} = 0$, 0.25, 0.5, 0.75, and 1), and the fluid proportion in the charge was always ~10% to ensure fluid saturation (see Supplementary Data Appendix 1; supplementary data are available for downloading at http://www.petrology.oxfordjournals.org). Once filled, capsules were weighed, crimped at their open end, arc welded shut with a graphite electrode, and then subsequently re-weighed to check for any mass loss or gain during welding. After welding, capsules were placed in an oven at 110°C for several minutes and then re-weighed to check for any leaks in the capsule. As a third method to check for leaks, some capsules were held in a beaker of oil at 300°C for a few seconds. If bubbles were observed escaping from the capsule, it was considered to have leaks and was thus discarded. After completion of the experiment, capsules were weighed to check that no fluid loss occurred during the run. Any capsules that showed a change in mass >0.2 mg either after welding or after heating were considered to have leaked at least part of their fluid phase and were discarded.

Experiments were run in vertically working internally heated pressure vessels (IHPVs; see Holloway, 1971) at the Institut des Sciences de la Terre Orléans (ISTO) at isothermal and isobaric conditions between 1000 and 1150°C and between 200 and 400 MPa with the oxygen fugacity of the vessel at about one log unit above the Ni–NiO buffer (NNO + 1; Table 2). Each run contained 5–10 sample capsules loaded into a vertically working IHPV equipped with a double-wound Kanthal furnace. An Ar–H_2 gas mixture loaded sequentially at room temperature was used as the pressure medium with the Ar/H_2 ratio fixed so as to achieve an experimental fO_2 in the vessel of NNO + 1 (Scaillet *et al.*, 1992),

Table 1: Composition of AW-82038 and KI-04 starting glass, whole-rock and representative analyses of phenocrysts and microphenocrysts in the natural rock

AW-82038	Whole-rock[1]	St. Gls[2]	Ol-6	Ol-10	Plag-5	Plag-12	Ap-1	Sp-1	gnd Ol-5	gnd Plag-5
SiO_2	48·01	48·03	38·72	38·47	54·10	53·69	0·26		36·27	55·46
TiO_2	2·77	2·84			0·14	0·15		26·18		0·16
Al_2O_3	18·56	18·12			28·54	29·24		4·34		28·56
FeO^*	9·49	9·59	20·47	22·54	0·35	0·31	0·33	63·15	29·08	0·39
MnO	0·22	0·23	0·28	0·45	0·00	0·04	0·10	0·80	0·64	0·03
MgO	3·18	3·08	41·79	39·84	0·03	0·03	0·26	5·29	35·09	0·05
CaO	7·65	7·57	0·30	0·30	11·11	11·53	55·11	0·04	0·44	10·62
Na_2O	5·99	6·04			4·90	4·66	0·07	0·04		5·20
K_2O	2·88	3·07			0·62	0·50				0·70
P_2O_5	1·24	1·41					42·02			
Total	98·29	99·54	101·72	101·80	99·82	100·21	98·16	100·04	101·74	101·19
Mg#	37	36	78	76					68	
Or					2·3	1·8				2·6
An					69·8	71·9				67·5
Ab					27·9	26·3				29·9

KI-04	Whole-rock[1]	St. Gls[2]	Ol-6	Ol-9	Aug-5	Aug-24	Plag-1	Plag-4
SiO_2	43·06	43·15	38·04	37·62	47·09	42·35	49·91	50·10
TiO_2	4·26	4·43			2·57	4·99	0·23	0·18
Al_2O_3	13·80	13·94			4·92	9·16	29·95	30·91
FeO	9·73	12·35*	17·61	19·83	7·98*	6·99*	0·66	0·53
Fe_2O_3	2·87							
MnO	0·19	0·17	0·22	0·31	0·25	0·10	0·00	0·00
MgO	8·92	8·46	43·56	40·66	13·34	12·10	0·10	0·09
CaO	11·07	11·16	0·29	0·39	22·49	22·70	14·11	14·62
Na_2O	3·64	3·81			0·46	0·45	3·41	3·31
K_2O	1·63	1·68					0·35	0·29
P_2O_5	0·83	0·85						
Total	98·61	97·68	100·00	98·99	99·10	99·06	98·72	100·04
Mg#	55	55	82	79	75	76		
Or							1·2	1·0
An							81·1	82·2
Ab							17·7	16·8

Glass analyses are given in wt % and normalized to 100% with original analysis totals given. Mineral analyses are not normalized; original analysis totals are given. St. Gls, starting glass after vitrification; Ol, olivine; Plag, plagioclase; Ap, apatite; Sp, spinel; gnd Ol, groundmass olivine; gnd Plag, groundmass plagioclase.
*Total iron given as FeO; Mg# $= 100[Mg/(Mg + Fe^*)]$ in mol %.
[1]Whole-rock composition. AW-82038 analyzed by Kyle *et al.* (1992); KI-04 analyzed in this study, using X-ray fluorescence (XRF).
[2]Electron microprobe (EMP) analyses of glass composition after vitrification in 1 atm furnace, but before run in pressure vessel. AW-82038 vitrified at an oxygen fugacity of NNO + 1 [analysis from Iacovino *et al.* (2013)]; KI-04 vitrified in air (analysis from this study).

although the fO_2 within each experimental charge varied slightly depending on its specific H_2O/CO_2 fluid mixture (see below). It is noteworthy that, because the experimental fO_2 is lower than that imposed during melting of the sample KI-04 starting material, some additional H_2O was created in the capsule during KI runs via the reduction of Fe^{3+}. Thus, even nominally 'dry' runs will contain some H_2O (typically < 1–2 wt %), and this has been taken into account for the calculation of experimental oxygen fugacity. Pressure was measured with a transducer calibrated against a Heise–Bourdon tube gauge with an accuracy of ±20 bars. Temperature was measured with two chromel–alumel (Type K) thermocouples, which allow for precise control over the length of the hotspot (~4 cm) to within ±5°C. Experiments were run for 17–24 h and then quenched by dropping the sample into the lower, cold part of the pressure vessel (<40°C), which gives a quench rate of >100°C s^{-1} (Roux & Lefevre, 1992). The very low

viscosities of our mafic alkalic glasses facilitated the attainment of equilibrium even given these relatively short run times. In similar studies on mafic melts, the attainment of equilibrium was observed in runs of similar duration (Di Carlo *et al.*, 2006; Feig *et al.*, 2010; Pichavant *et al.*, 2014).

ANALYTICAL TECHNIQUES

Fluid phase composition

For capsules that did not leak, the conventional weight-loss method was employed as a first-order measure of the composition of the equilibrium H_2O–CO_2 fluid phase (see Behrens *et al.*, 2009). After the first post-run weighing, the capsule was submerged in a liquid nitrogen bath, thus freezing any liquid water or water vapor but allowing the CO_2 to remain as a gas. The capsule was then punctured to allow for the escape of the CO_2 gas, and a hissing noise and bubbles at the puncture site
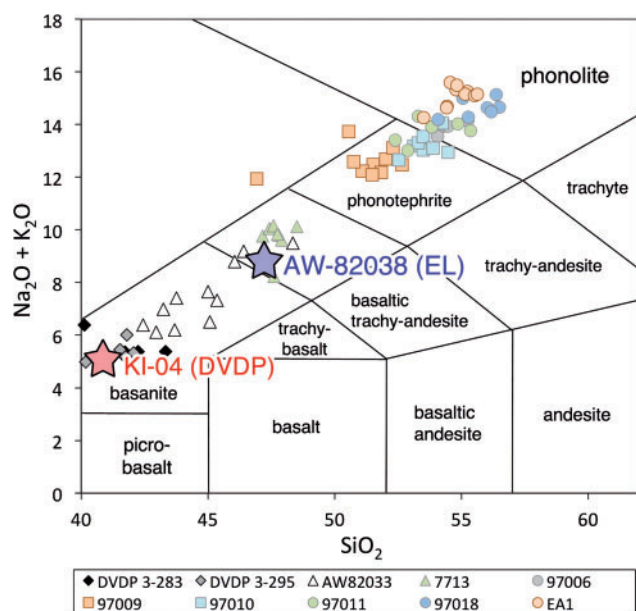
Fig. 3. Total alkalis vs silica (TAS) diagram showing the compositions of the starting materials (stars) relative to the fractional crystallization sequence seen in Erebus Lineage rocks represented by a suite of melt inclusions [data from Oppenheimer *et al.* (2011)].

were typically observed. After warming at room temperature for up to 1 min, the capsule was weighed to determine the mass of CO_2 lost after puncture. This was then recorded as the mass of CO_2 in the fluid phase. The capsule was then placed in a drying oven at 110°C for several minutes to evaporate the remaining H_2O and then weighed to determine the mass of the H_2O fluid. During this step, capsule weight was checked periodically until its mass remained constant. It should be noted that this method is an indirect measure of the composition of the fluid phase in our runs and can be prone to significant error owing to uncertainties in the weighing of the capsules before and after opening. Behrens *et al.* (2009) estimated an error in XH_2O determination of around ±0·03 using this method. The composition of the fluid phase was also calculated by mass balance, where the mass of dissolved H_2O or CO_2 in the glass [as measured by Fourier transform IR (FTIR) spectroscopy] is subtracted from the amount of fluid (liquid H_2O or CO_2 as silver oxalate) added to the capsule (see Supplementary Data Appendix 1). A comparison of fluid compositions calculated both by weight loss and by mass balance shows reasonable agreement, with a correlation coefficient between the two methods of $R = 0·79$ and an average error in XH_2O determination between the two methods of ±0·11. Here, calculation of the fluid phase composition by weight loss is preferred, with the mass-balance method used for sample KI-07, for which weight-loss data were not obtained. After fluid mass measurement, the AuPd capsule was peeled away, and the sample was mounted in epoxy and polished for analysis. Selected samples were doubly polished for analysis by FTIR spectroscopy.

SEM and electron microprobe

Charges were initially studied using a JEOL WINSET JSM 6400 scanning electron microscope (SEM) at ISTO for preliminary phase identification, modal abundance determination and textural analysis. Most phases could be identified by visual inspection, and several crystals from each phase were analysed using energy-dispersive spectrometery (EDS). The EDS analyses are not reported here as they were used only for mineral identification.

Representative SEM images from each sample were digitally processed to measure total crystallinity and the modal abundance of all phases. Images were converted to grayscale and a threshold was applied and adjusted to isolate each phase. The total area of each phase was then calculated as a percentage of the total image. Any areas of the image that contained no sample (holes, cracks, etc.) were not included in the total sample area.

Electron microprobe (EMP) analyses of the major element compositions of the glass and crystal phases in the natural samples, starting glasses and experimental run products were made primarily using a Cameca SX-100 electron microprobe at the University of Cambridge. Some samples were analyzed on a Cameca SX-100 at the University of Arizona or on a Cameca SX-50 at the Università degli Studi di Padova. Glass was measured using an accelerating voltage of 15 keV, a beam current of 3 nA, a defocused beam size of 10 μm, and a peak counting time of 10 s, analyzing Na first to minimize any measurement error owing to Na migration. Crystal phases were analyzed with an accelerating voltage of 15 keV, a beam current of 10 nA, a focused beam with a diameter of 1 μm, and a peak counting time of 20 s. In each experimental charge, typically 20–30 analyses were performed on glass and 8–12 analyses were performed on each crystal phase.

FTIR spectroscopy

Whenever possible, the H_2O and CO_2 concentrations in the glass phase of each experimental charge were measured using a Thermo Scientific Nicolet iN10 MX mapping FTIR system at the US Geological Survey in Menlo Park, California. Transmission IR spectra of doubly polished glass chips ranging in thickness from ~20 to 150 μm were obtained in the 6000–1000 cm^{-1} wavenumber range using a KBr beamsplitter with a variable aperture size between 25 and 500 μm^2. The sample stage was continuously purged with dry air, and a background measurement was made before the collection of each spectrum to minimize and correct for the contribution of atmospheric H_2O and CO_2. Moderately to highly crystal-rich charges were characterized with FTIR mapping to identify crystal-free regions for the analysis of dissolved volatiles.

The concentrations of OH, H_2O, CO_2, and CO_3 species were calculated with the Beer–Lambert Law (Ihinger *et al.*, 1994), using near-IR (4500 and 5200 cm^{-1}), total water (3500 cm^{-1}), molecular H_2O (1640 cm^{-1}), CO_2

Table 2: Experimental conditions and run products

Run	Experiment	P (MPa)	T (°C)	$X\mathrm{H2O}^{\text{in 1}}$	$X\mathrm{H_2O}^{\text{fluid 2}}$	H_2O glass (wt %)[3]	CO_2 glass (ppm)[3]	fO_2 (ΔNNO)[4]	Phases (vol. %)[5]
AW 82038 phonotephrite experiments									
PV-4B	AW-19B	200	1000	0·18	0·14	0·49	—	0·9	Gl 5, Cpx 10, Plag 81, Tit 3, Ap 1
PV-4B	AW-20B	200	1000	0·49	0·35	1·79	1077	1·7	Gl 81, Kaers 16, Tit 3
PV-4B	AW-21	200	1000	0·72	0·56	3·22 (23)	931	2·1	Gl 87, Kaers 9, Tit 4
PV-4B	AW-22	200	1000	0·88	0·74	4·04 (37)	817	2·4	Gl 87, Kaers 8, Tit 5
PV-4B	AW-23	200	1000	1·00	1·00	5·55 (10)	0	2·6	Gl 96, Tit 4
PV-3	AW-06	200	1050	—	—	1·42 (7)	1298 (137)	—	Gl 92, Plag 7, Tit < 1
PV-3	AW-17	200	1050	0·75	0·43	3·14 (11)	443 (17)	1·2	Gl 99, Tit 1
PV-3	AW-18	200	1050	0·87	0·71	4·00[6]	—	1·6	Gl 99, Tit 1
PV-3	AW-10	200	1050	1·00	1·00	5·57 (11)	0	1·9	Gl 99, Tit 1, Ap < 1
PV-2	AW-14	200	1100	0·78	0·20	1·86	831	1·2	Gl 99, Tit 1
PV-2	AW-13	200	1100	0·91	0·68	4·27 (20)	937	2·3	Gl 99, Tit 1
PV-8	AW-24B	250	1100	0·21	0·13	1·14 (1)	1700 (74)	1·0	Gl 100
PV-11	AW-42	300	1000	0·21	0·22	0·73 (3)	1145 (107)	1·6	Gl 78, Kaers 13, Plag 2, Tit 7
PV-11	AW-41	300	1000	0·49	0·49	1·78	1180	2·3	Gl 80, Kaers 15, Tit 5
PV-11	AW-40	300	1000	0·72	0·64	2·75 (34)	1975 (329)	2·6	Gl 94, Kaers 2, Tit 4
PV-11	AW-39	300	1000	0·86	0·86	4·30 (16)	1227 (366)	2·8	Gl 91, Tit 9, Ap < 1
PV-11	AW-38	300	1000	1·00	1·00	7·26 (22)	0	3·0	Gl 95, Tit 5
PV-6	AW-29	300	1050	0·18	—	1·01 (3)	1653 (150)	—	Gl 93, Plag 7
PV-6	AW-33	300	1050	0·73	0·71	2·94 (6)	1702 (358)	1·9	Gl 99, Tit 1
PV-6	AW-34	300	1050	1·00	1·00	5·90 (78)	0	2·2	Gl 97, Tit 3
PV-10	AW-37	300	1100	0·21	0·14	0·17[6]	—	1·2	Gl 99, Tit 1
PV-5	AW-25	300	1100	0·53	0·25	2·25 (9)	1186 (97)	1·7	Gl 99, Tit < 1
PV-5	AW-27	300	1100	0·88	0·67	3·03 (1·13)	1622 (311)	2·6	Gl 99, Tit < 1
PV-5	AW-26	300	1100	0·75	0·43	3·59 (3)	982 (59)	2·2	Gl 99, Tit < 1
PV-5	AW-28	300	1100	1·00	1·00	6·65 (85)	0	3·0	Gl 99, Tit < 1
PV-15	AW-43	400	1000	0·21	0·18	0·02[6]	—	1·7	Gl 36, Cpx 22, Plag 35, Tit 7
PV-15	AW-44	400	1000	0·49	0·51	2·21	—	2·6	Gl 75, Kaers 19, Tit 6
PV-15	AW-45	400	1000	0·70	0·71	4·04 (13)	3375 (824)	2·9	Gl 80, Kaers 13, Tit 7
PV-15	AW-46	400	1000	0·86	0·74	4·76 (76)	3439 (134)	2·9	Gl 87, Kaers 9, Tit 4
PV-15	AW-47	400	1000	1·00	1·00	6·84 (49)	0	3·2	Gl 74, Tit 26
KI-04 basanite experiments									
PV-7	KI-09	200	1050	0·19	0·17	0·73 (17)	1154 (271)	0·4	Gl 70, Cpx 23, Tit 7
PV-7	KI-10	200	1050	0·75	0·55	1·52 (11)	1233 (137)	1·4	Gl 53, Cpx 44, Tit 3 + rare Ol
PV-7	KI-11	200	1050	0·70	0·60	2·18[6]	—	1·4	Gl 60, Kaers 37, Tit 4
PV-7	KI-12	200	1050	0·86	0·78	3·55[6]	—	1·7	Gl 65, Ol 6, Cpx 25, Tit 5
PV-2	KI-05	200	1100	1·00	—	—	—	—	All quench
PV-2	KI-06	200	1100	0·89	—	—	—	—	Quench + rare Ol
PV-2	KI-08	200	1100	0·58	—	—	—	—	Gl 86, Ol 11, Tit 2
PV-2	KI-07	200	1100	0·76	0·58	2·90 (8)	1131 (100)	2·2	Gl 93, Ol 4, Tit 3
PV-8	KI-14	250	1100	0·17	0·20	0·45[6]	—	1·4	Gl 52, Ol 26, Cpx 23
PV-8	KI-15	250	1100	0·49	0·43	1·91 (2)	3074 (627)	2·1	Gl 91, Ol 9, Tit < 1
PV-8	KI-16	250	1100	0·69	0·54	3·33	4338	2·3	Gl 72, Ol 27, Tit 1
PV-8	KI-17	250	1100	0·87	0·77	3·84[6]	—	2·6	Gl 58, Ol 21
PV-8	KI-18	250	1100	1·00	1·00	—	—	2·8	All quench
PV-10	KI-23	300	1100	0·21	0·14	1·11 (4)	2628 (257)	1·2	Gl 80, Ol 15, Q 5
PV-10	KI-22	300	1100	0·49	0·26	2·13[6]	—	1·8	Gl 92, Ol 8, Tit < 1
PV-10	KI-21	300	1100	0·70	0·48	2·79 (58)	2798 (573)	2·3	Gl 91, Ol 9, Tit < 1
PV-10	KI-20	300	1100	0·87	0·61	2·21 (31)	1256 (364)	2·5	Gl, Q + rare Ol
PV-10	KI-19	300	1100	1·00	1·00	—	—	3·0	All quench
PV-12	KI-28	300	1150	0·21	0·21	0·59[6]	—	0·9	Gl 98, Ol 2, Tit < 1
PV-12	KI-27	300	1150	0·49	0·32	1·80[6]	—	1·3	Gl 99, Ol 1, Tit < 1
PV-12	KI-26	300	1150	0·70	0·43	—	—	1·6	All quench
PV-12	KI-25	300	1150	0·86	0·83	—	—	2·2	All quench
PV-12	KI-24	300	1150	1·00	1·00	—	—	2·3	All quench
PV-13	KI-29	400	1000	0·21	0·13	—	—	1·4	Subsolidus
PV-13	KI-30	400	1000	0·48	0·31	—	—	2·1	Subsolidus
PV-13	KI-31	400	1000	0·71	0·59	2·72[6]	—	2·7	Gl 38, Kaers 60, Tit 2
PV-13	KI-32	400	1000	0·85	0·80	3·05 (5)	1601 (139)	3·0	Gl 57, Kaers 41, Tit 2

(continued)

Table 2: Continued

Run	Experiment	P (MPa)	T (°C)	XH2O[in 1]	XH$_2$O[fluid 2]	H$_2$O glass (wt %)[3]	CO$_2$ glass (ppm)[3]	fO$_2$ (ΔNNO)[4]	Phases (vol. %)[5]
PV-13	K1-33	400	1000	1·00	1·00	4·30[6]	0	3·2	Gl 38, Kaers 59, Tit 3
PV-14	KI-36	400	1100	0·72	0·53	3·38[6]	—	2·6	Gl 95, Ol 5, Tit < 1
PV-14	KI-37	400	1100	0·85	0·80	3·56[6]	—	3·0	Gl 29, Q 51, Ol 20
PV-14	KI-38	400	1100	1·00	1·00	—	—	3·2	All quench

[1]Mole fraction of H$_2$O in the H$_2$O–CO$_2$ fluid added to the experimental capsule prior to running at P and T.
[2]Mole fraction of H$_2$O in the equilibrium H$_2$O–CO$_2$ fluid phase during the run, measured by weight-loss method. Sample KI-07 calculated by mass balance.
[3]Weight per cent H$_2$O or ppm CO$_2$ dissolved in the glass, measured via FTIR spectroscopy. Standard deviation shown in parentheses.
[4]Calculated oxygen fugacity of the experiment in terms of ΔNNO (log units from the Ni–NiO buffer). (See text for details.)
[5]Phase proportions calculated as volume per cent; Gl, glass; Ol, olivine; Cpx, clinopyroxene; Kaer, kaersutite; Fsp, feldspar; Ap, apatite; Tit, titanomagnetite; Q, quench crystals.
[6]Volatile concentration calculated by mass balance using values in Table 3. Corrected values using the calibration lines in Supplementary Data Fig. A2.2 are reported here.

Table 3: Absorption coefficients used to determine concentrations of dissolved volatiles in experimental charges via FTIR spectroscopy

Composition and wavenumber (cm^{-1})	Species	Coefficient [l (mol cm)$^{-1}$]	Reference
Phonolite			
1640	H$_2$O$_m$	25 ± 3	Dixon *et al.*, 1994
2345	CO$_2$	890	Morizet *et al.*, 2002
3500	H$_2$O^{tot}	64 ± 8	Cioni, 2000
Tephriphonolite			
1430	CO$_3$	Calculated	Dixon & Pan, 1995
1525	CO$_3$	Calculated	Dixon & Pan, 1995
1640	H$_2$O$_m$	25 ± 3	Dixon *et al.*, 1994
3500	H$_2$O^{tot}	64 ± 8	Cioni, 2000
4500	OH	0·62 ± 0·02	Behrens *et al.*, 2009
5200	H$_2$O$_m$	1·02 ± 0·06	Behrens *et al.*, 2009
Phonotephrite			
1430	CO$_3$	Calculated	Dixon & Pan, 1995
1525	CO$_3$	Calculated	Dixon & Pan, 1995
1640	H$_2$O$_m$	25 ± 3	Dixon *et al.*, 1994
3500	H$_2$O^{tot}	63·9 ± 5·4	Behrens *et al.*, 2009
4500	OH	0·62 ± 0·02	Behrens *et al.*, 2009
5200	H$_2$O$_m$	1·02 ± 0·06	Behrens *et al.*, 2009
Basanite			
1430	CO$_3$	375 ± 20	Fine & Stolper, 1986
1525	CO$_3$	375 ± 20	Fine & Stolper, 1986
1640	H$_2$O$_m$	25 ± 3	Dixon *et al.*, 1994
3500	H$_2$O^{tot}	63·9 ± 5·4	Behrens *et al.*, 2009
4500	OH	0·58 ± 0·02	Cocheo, 1993
5200	H$_2$O$_m$	0·56 ± 0·04	Cocheo, 1993

(2345 cm^{-1}), and carbonate (1430 and 1525 cm^{-1}) bands. The total water 3500 cm^{-1} band was always preferred for retrieving H$_2$O concentrations; in five samples the peak at this band was unusable and so near-IR bands were used. The H$_2$O concentrations in samples measured with both the total water and near-IR bands agree well, with an average standard deviation of 0·57 wt % and an R^2 value of 0·83.

Sample thicknesses were measured to an accuracy of ±2 μm using a digital tabletop micrometer equipped with a fine tip that allowed for measurement at multiple spots on the sample surface. Additional sample thicknesses for some samples were also measured using an ADE Phaseshift Microxam surface-mapping microscope (with white light interferometer) to an accuracy of ±0·5–2 μm. In very thin samples, the presence of interference

fringes in reflectance IR spectra allowed for the measurement of the sample thickness in the precise spot that was analyzed with transmitted light, following the method of Nichols & Wysoczanski (2007, and references therein; see Supplementary Data Appendix 2 for details).

Glass densities were calculated for each sample using the model of Lange & Carmichael (1987), assuming an H$_2$O molar volume of 22·9 cm^3 mol^{-1} (Ochs & Lange, 1999). Molar absorption coefficients strongly depend on glass composition (Pandya *et al.*, 1992). Because of variation in the crystallinity of our samples, and therefore significant variation in glass chemistry, an attempt was made to use absorption coefficients appropriate for each sample. All absorption coefficients used in this study are listed in Table 3. Where possible, the model of Dixon & Pan (1995) was used to calculate ε_{1525} and ε_{1430} (carbonate absorption) for single samples. This calculation can only be applied to glasses with an Na/(Na + Ca) ratio between 0·25 and 0·5 (in our case, most glasses classified as phonotephrite and tephriphonolite fall in this range). For glasses with Na/(Na + Ca) < 0·25 or > 0·5, ε_{1525} and ε_{1430} values were selected from the literature (see Table 3). (See Supplementary Data Appendix 2 for details of FTIR spectral background fitting, absorbance measurements, sample thicknesses, and glass density calculations.)

Dissolved volatile concentrations could not be measured in nine crystalline samples (29–75 vol. % glass) where glass pools were too small to analyze by FTIR spectroscopy. A further six glassy samples (95–99 vol. % glass) could not be successfully prepared for FTIR analysis. For these 15 samples, H$_2$O and CO$_2$ contents were calculated using the mass-balance method (see Supplementary Data Appendices 3 and 4 for details), and the 35 samples for which FTIR measurements were obtained were used as internal standards. The standard error for these calculations is large at ±1·4 wt % and ±1000 ppm for calculated H$_2$O and CO$_2$ values, respectively.

Oxygen fugacity

The fO_2 of all IHPV runs was controlled by loading the pressure vessel with sufficient H_2 to achieve an apparatus fO_2 of $\sim NNO + 1$. The fO_2 inside each experimental capsule will vary depending on the H_2O/CO_2 ratio of the fluid phase contained therein. Assuming that the fH_2 of the pressure vessel will be the same as the fH_2 inside an experimental capsule owing to the very fast diffusion rates of hydrogen, we can calculate the fO_2 inside each capsule following the method of Iacovino *et al.* (2013*a*). First, because the partial pressure of H_2 is fixed for each experiment, we can calculate the fH_2 of the pressure vessel for each run using the equation

$$fH_2 = \phi P_{H2} \tag{1}$$

where ϕ is the fugacity coefficient of hydrogen for the P and T of a given experiment (Shaw & Wones, 1964), and P_{H2} is the partial pressure of hydrogen gas added to the IHPV at the start of the run. If the XH_2O^{fluid} is known, we can also then calculate the fH_2O inside the capsule as

$$fH_2O^{inside} = fH_2O^{pure} XH_2O^{fluid} \tag{2}$$

where fH_2O^{pure} is the fugacity of pure H_2O vapor at the experimental P and T conditions, assuming ideal mixing between H_2O and CO_2 in the fluid [calculated with the modified Redlich–Kwong equation of state of Holloway (1977) as modified by Flowers (1979)]. Now, it is possible to calculate the oxygen fugacity for each experiment as follows:

$$fO_2^{inside} = \left(\frac{fH_2O^{inside}}{fH_2 K_F} \right)^2 \tag{3}$$

where K_F is the equilibrium constant of formation for H_2O (Robie *et al.*, 1979). Oxygen fugacities in our experiments are reported in Table 2 and range from a ΔNNO of $+0.3$ to $+3.2$.

RESULTS

Textural and mineralogical observations

Optical and electron microscope images revealed homogeneously distributed euhedral crystals in most experimental charges, with crystals ranging in size from $<5\,\mu m$ to $\sim 80\,\mu m$ in length. Phases identified include olivine, clinopyroxene, plagioclase, amphibole, Fe–Ti oxides, apatite, glass and fluid inclusions. In the most highly crystalline charges, glass tends to collect in pools and small subhedral crystals ('quench' texture) are ubiquitous. Quench texture is especially common in KI samples with high H_2O contents, probably owing to the extremely low-viscosity melt allowing for the rapid crystallization upon quench. In samples where crystals were too small to analyze by electron microprobe ($<25\,\mu m^2$), phases were analyzed quantitatively for identification purposes only. Those analyses are not reported here.

Phase relationships

The equilibrium phase relations for the AW and KI experiments are shown in Figs 4 and 5. In both compositions, titanomagnetite is ubiquitous in nearly all experimental charges independent of $P/T/H_2O$ and is probably stabilized owing to the relatively oxidizing conditions of our experiments. Experiments are plotted in terms of the mole fraction of H_2O in the $H_2O–CO_2$ fluid added to the capsule, XH_2O^{in}.

In AW, kaersutite is the liquidus phase at median to high water contents, crystallizing below about $1025^\circ C$. Amphibole is common in the AW experiments and is stable to melt H_2O contents as low as $\sim 1\,wt\%$. A reaction relationship between kaersutite and clinopyroxene is inferred to exist around $XH_2O^{fluid} = 0.1–0.2$, below which clinopyroxene is the dominant calcic ferromagnesian phase (experiments AW-19B and AW-43). As with kaersutite, clinopyroxene is restricted to below about $1025^\circ C$. Plagioclase feldspar is the dry liquidus phase and is restricted to low water contents, with its stability field increasing with decreasing temperature. Phase equilibria at 300 MPa are similar to those at 200 MPa [the stability field for clinopyroxene at 300 MPa (Fig. 4b) is inferred based on that at 200 MPa (Fig. 4a)]. Although apatite was not always detected, it is inferred to crystallize below $1100^\circ C$ at both pressures. Its stability is mostly constrained by water-saturated experiments, but apatite is probably stable but undetectable in drier runs (see Harrison & Watson, 1984). This hypothesis is supported by the steady decrease in the P_2O_5 content of residual liquids in phonotephrite experiments. The polybaric section at $1000^\circ C$ (Fig. 4c) shows that in the pressure range 200–400 MPa amphibole is always the liquidus phase, followed by Pl and Cpx, in that order.

In KI experiments at 200 MPa (Fig. 5a), olivine is the liquidus phase followed by clinopyroxene and kaersutite. Although loosely constrained, the liquidus is located above $1100^\circ C$ except at very high H_2O contents (XH_2O^{in} approaching unity), where it drops to $\sim 1075^\circ C$. A peritectic-like relationship exists at intermediate melt water contents and $1050^\circ C$ at 200 MPa where olivine is replaced by kaersutite at low temperatures. At these $P–T$ conditions, clinopyroxene replaces kaersutite as the dominant ferromagnesian phase at low and high melt water contents where it coexists with olivine, except at very low melt water contents (XH_2O^{in} approaching zero) where clinopyroxene is the only stable silicate phase. The phase relationships observed at 400 MPa (Fig. 5b) are broadly similar to those at 200 MPa except that the kaersutite stability field is enlarged towards H_2O-rich conditions, this mineral being in reaction relationships with both olivine and clinopyroxene as temperature decreases. The polybaric section at $1100^\circ C$ (Fig. 5c) illustrates that olivine is the liquidus mineral in the pressure range 200–400 MPa, for a large range of fluid compositions (melt water content), followed by clinopyroxene at $XH_2O_{in} < 0.25$.
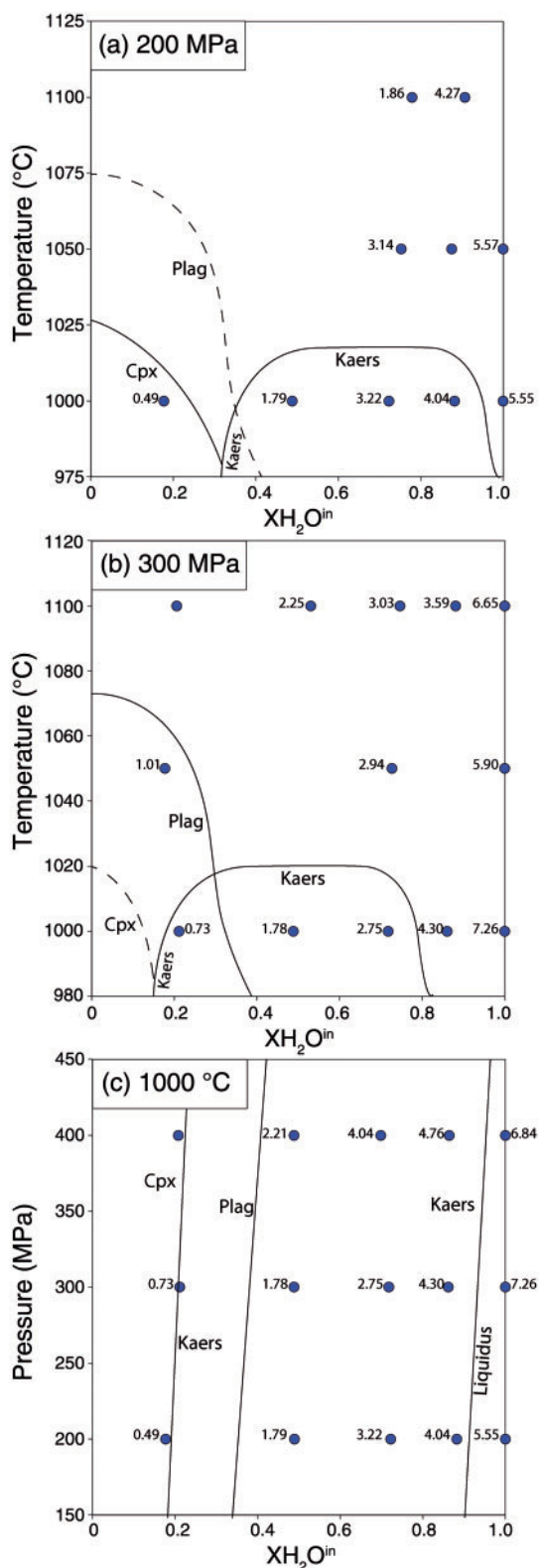
Fig. 4. Isothermal (a, b) and isobaric (c) phase diagrams illustrating the stability fields of different phases in AW experiments. Numbers next to points indicate wt % H_2O dissolved in the glass of the experimental charge as measured by FTIR spectroscopy. Although not shown, titanomagnetite is ubiquitous in all charges. Apatite was not always detected but is inferred to be stable in runs below ~1100°C. A dashed line indicates an inferred phase boundary.
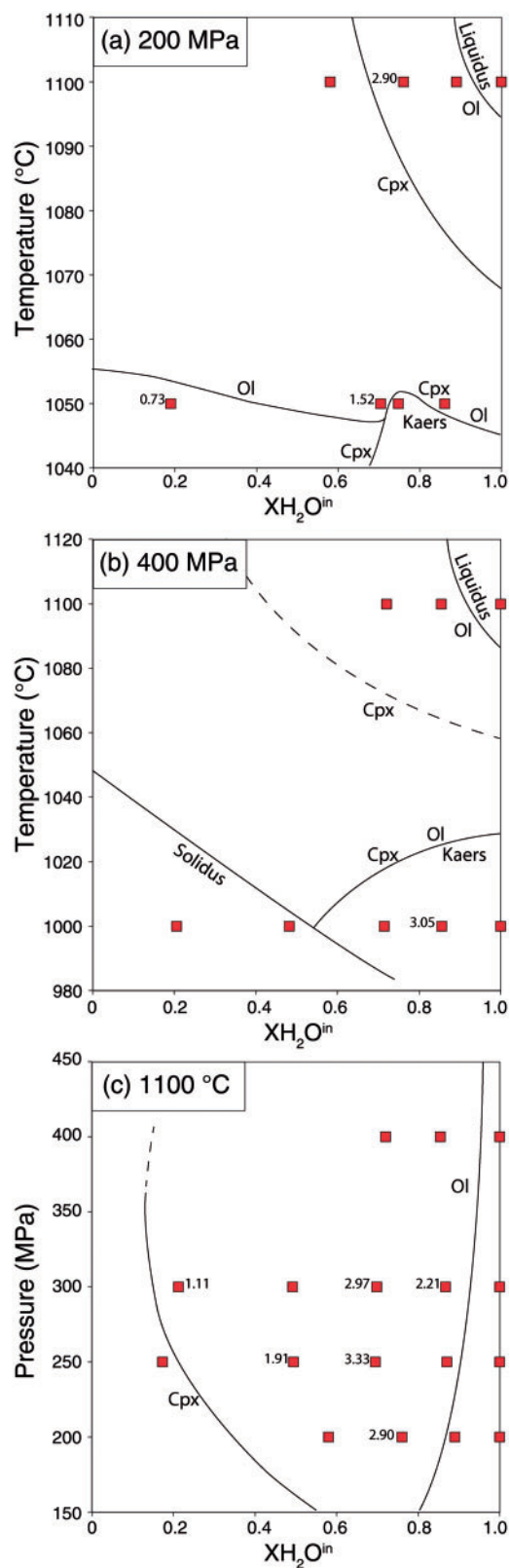
Fig. 5. Isothermal (a, b) and isobaric (c) phase diagrams illustrating the stability fields of different phases in KI experiments. Numbers next to points indicate wt % H_2O dissolved in the glass of the experimental charge as measured by FTIR spectroscopy. Although not shown, titanomagnetite is ubiquitous in all charges. Apatite was not always detected but is inferred to be stable in runs below ~1100°C. A dashed line indicates an inferred phase boundary.

Experimental phase compositions

Compositions of the experimental mineral phases and residual glasses are given in Table 4. Chemical analyses for all natural and experimental phases are given in Supplementary Data Appendix 5. Titanomagnetite, apatite, and some clinopyroxene crystals were too small to be analyzed by electron microprobe ($<25\,\mu m^2$). In six charges, clinopyroxenes were large enough to be analyzed, and their compositions are reported in Table 4. In most samples, the $K_D^{Fe–Mg}$ values of experimental clinopyroxenes, which range from 0·31 to 0·46 and average 0·36 (calculated using Fe^{2+} as $XFeO$), are similar to the $K_D^{Fe–Mg}$ values observed in natural KI-04 basanite clinopyroxenes, which average 0·40, suggesting equilibrium crystal growth. Overall, clinopyroxene is characterized by elevated contents of Al_2O_3 and TiO_2, which do not show any obvious correlation with experimental parameters in the explored range.

Experimental olivine compositions in KI range from Fo_{77} to Fo_{90} (Table 4). No olivine crystals were observed in AW experimental samples. Experimental olivine Fo contents become more forsteritic with increasing H_2O^{melt} (Fig. 6), reflecting the increase in the melt fraction of the charge and a change in oxygen fugacity caused by an increase in the water activity in the melt (e.g. Feig *et al.*, 2010). Crystal–melt Fe–Mg partition coefficients (K_D) for most experimental olivines range from 0·33 to 0·39, with an overall average value (including outliers) of 0·33. Our olivines are expected to have a higher K_D value than the canonical 0·3 owing to the alkalinity and redox state of the charges. Using the model of Carmichael & Ghiorso (1990), which accounts for the effect of melt composition on K_D, we calculate that our experimental K_D values should range between 0·34 and 0·36, suggesting that the majority of the olivine crystals in our experiments are approaching equilibrium with their host melts. Four outliers, which do not appear to have attained equilibrium, are samples KI-06 ($K_D = 0·22$), KI-08 (0·22), KI-10 (0·52), and KI-36 (0·43). In samples KI-06 and KI-10, olivines were rare and small, suggesting that they grew late during the experiment, possibly during quench. Some olivines may have been affected by Fe loss to the experimental capsule, which is difficult to avoid at high T even given the relatively short run times of 24 h.

Amphibole is classified as sodic-kaersutite on the basis of 23 oxygens and crystallized in both phonotephrite and basanite experiments (compositions reported in Table 4). Al contents in kaersutites show a positive correlation with pressure, as documented for other systems (e.g. Prouteau & Scaillet, 2003) but in contrast to the results of experiments with Erebus phonolite (Moussallam *et al.*, 2013). Kaersutites synthesized at the lowest fO_2 conditions have markedly lower Mg# and higher Ti contents. At all pressures, the modal proportion of amphibole in AW runs increases as the water content of the melt decreases.

Plagioclase feldspar was observed only in the driest AW experiments and ranges from An_{57} to An_{65}. It was not found in any of the KI experiments.

Glass compositions

The compositions of residual experimental glasses highlight the evolution of the melts from the starting composition to intermediate and evolved compositions. FeO, MgO, CaO, and TiO_2 all show continuously decreasing trends with melt evolution reflecting the crystallization of pyroxene or kaersutite, olivine, plagioclase, and titanomagnetite. In contrast, Al_2O_3, and K_2O show continuously increasing trends. In detail, Harker-type plots clearly show the effect of the fractionating assemblage on the liquid lines of descent of each starting material (Figs 7 and 8).

KI-related melts in charges held above 1050°C show limited compositional evolution relative to the starting composition, except for FeO and MgO contents, which are affected by olivine and titanomagnetite crystallization to some extent. In contrast, charges held at or below 1050°C show the prominent roles of either kaersutite or Cpx–Ol-dominated assemblages. In both cases, derivative liquids produced by crystallization at these temperatures reach SiO_2 contents of 50–52 wt % (i.e. are more evolved than the AW starting composition), trending toward the phonotephritic to phonolitic fields. Charges in which kaersutite is stable are characterized by higher TiO_2, FeO, and CaO melt contents relative to those in which Cpx and Ol are stable (at the same SiO_2 content). In contrast, the crystallization of a Cpx ± Ol assemblage produces liquids with higher Al_2O_3, Na_2O, and K_2O contents relative to those in which kaersutite predominates. It is worth noting that the role of kaersutite increases at high pressure; charges crystallized at 400 MPa have up to 60 wt % amphibole, whereas at 200 MPa, amphibole does not exceed 37 wt % of the crystal cumulate (Table 2).

The relationship between the evolution of CaO and MgO in KI liquids is illustrated in Fig. 9. Such a plot is useful for illuminating the evolution of basaltic compositions *sensu lato* in which olivine and Ca-pyroxene (or amphibole) play a dominant role (e.g. Pichavant *et al.*, 2009, 2014). The KI trend can be divided into two segments: the first runs broadly parallel to the MgO axis, primarily reflecting depletion in MgO of the liquid owing to olivine crystallization. The second segment corresponds to liquids in which either kaersutite or Cpx ± Ol crystallize, defining either a kaersutite control line or the Cpx–Ol cotectic (at 1050°C), along which both CaO and MgO contents decrease. It is apparent that liquids lying on the Cpx–Ol cotectic are slightly less CaO-rich than those driven by kaersutite crystallization. Also shown in Fig. 9 are the Cpx–Ol cotectics experimentally determined for Stromboli and Vesuvius primitive basalts (Di Carlo *et al.*, 2006; Pichavant *et al.*, 2009, 2014), which, like the magma compositions investigated here, are mafic and alkali-rich. It is clear that basaltic liquids

Table 4: Compositions of experimental phases

Phase	SiO$_2$	TiO$_2$	Al$_2$O$_3$	FeO^T	MnO	MgO	CaO	Na$_2$O	K$_2$O	P$_2$O$_5$	Total	Mol %
AW 82038 experiments												
AW-6 PT (9)	48.03 (0.74)	2.84 (0.24)	18.12 (0.62)	9.60 (0.89)	0.23 (0.05)	3.08 (0.28)	7.57 (0.38)	6.04 (0.12)	3.08 (0.11)	1.41 (0.22)	99.20 (0.59)	Mg no. 36.4
plag (4)	50.38 (0.9)	1.75 (0.30)	22.74 (1.26)	5.29 (0.85)	0.13 (0.04)	1.62 (0.34)	8.83 (0.31)	5.00 (0.20)	1.89 (0.28)	n.d.	97.64 (0.54)	An$_{61}$Al$_{31}$Or$_8$
AW-10 PT (7)	49.45 (0.3)	2.64 (0.07)	18.74 (0.26)	8.26 (0.36)	0.25 (0.04)	2.73 (0.07)	7.62 (0.07)	5.98 (0.09)	3.08 (0.11)	1.26 (0.03)	95.00 (0.69)	Mg no. 37.1
AW-13 PT (9)	48.84 (0.44)	2.74 (0.07)	18.64 (0.24)	8.89 (0.27)	0.23 (0.04)	2.84 (0.10)	7.64 (0.11)	5.89 (0.11)	3.00 (0.06)	1.30 (0.05)	96.08 (0.80)	Mg no. 36.3
AW-14 PT (7)	48.75 (0.49)	2.72 (0.08)	18.59 (0.15)	8.94 (0.34)	0.18 (0.04)	2.89 (0.08)	7.63 (0.13)	5.99 (0.12)	2.99 (0.07)	1.31 (0.06)	97.08 (0.72)	Mg no. 36.6
AW-17 PT (7)	49.29 (0.26)	2.63 (0.08)	18.75 (0.17)	8.43 (0.36)	0.21 (0.02)	2.85 (0.07)	7.59 (0.19)	5.94 (0.17)	3.03 (0.07)	1.29 (0.06)	97.52 (0.43)	Mg no. 37.7
AW-18 PT (7)	49.60 (0.41)	2.56 (0.14)	18.76 (0.28)	8.21 (0.16)	0.21 (0.04)	2.89 (0.11)	7.60 (0.08)	5.96 (0.15)	2.97 (0.09)	1.24 (0.05)	96.41 (0.51)	Mg no. 38.5
AW-19B P (4)	53.74 (0.87)	1.53 (0.04)	19.46 (0.10)	4.05 (0.29)	0.15 (0.07)	1.03 (0.11)	4.21 (0.23)	8.29 (0.23)	5.87 (0.09)	1.68 (0.21)	96.63 (0.70)	Mg no. 31.1
cpx (4)	45.09 (1.3)	3.45 (0.51)	7.75 (0.45)	8.01 (0.47)	0.34 (0.02)	11.19 (0.30)	21.17 (0.71)	1.16 (0.13)	0.26 (0.17)	n.d.	98.43 (0.65)	En$_{36}$Wo$_{49}$Fe$_{15}$
plag (1)	55.16	1.06	22.61	3.8	0.1	1.64	9.72	5.07	1.26	n.d.	100.43	An$_{65}$Al$_{30}$Or$_5$
AW-20B T (10)	55.30 (0.64)	1.72 (0.04)	19.86 (0.49)	4.25 (0.25)	0.20 (0.07)	1.30 (0.09)	4.15 (0.33)	8.05 (0.13)	4.74 (0.23)	0.44 (0.19)	94.76 (1.30)	Mg no. 35.3
kaers (7)	37.38 (0.91)	6.33 (0.35)	12.68 (0.41)	10.32 (0.55)	0.23 (0.04)	12.12 (0.36)	11.33 (0.64)	2.76 (0.05)	1.18 (0.08)	0.12 (0.10)	94.48 (2.32)	Mg no. 67.7
AW-21 T (10)	53.93 (0.44)	2.01 (0.07)	20.07 (0.36)	4.79 (0.28)	0.20 (0.08)	1.56 (0.09)	5.80 (0.19)	7.36 (0.15)	3.80 (0.08)	0.48 (0.19)	94.24 (0.84)	Mg no. 36.7
kaers (6)	36.75 (0.56)	5.96 (0.28)	13.58 (0.44)	10.92 (0.33)	0.23 (0.06)	11.97 (0.23)	11.92 (0.09)	2.64 (0.08)	1.09 (0.08)	0.25 (0.33)	95.35 (0.77)	Mg no. 66.1
AW-22 T (12)	52.51 (0.58)	2.37 (0.07)	19.69 (0.17)	5.23 (0.21)	0.22 (0.05)	2.24 (0.10)	7.12 (0.14)	6.57 (0.13)	3.47 (0.11)	0.59 (0.17)	92.11 (0.71)	Mg no. 43.3
kaers (10)	37.56 (0.69)	5.27 (0.23)	13.00 (0.37)	10.15 (0.17)	0.16 (0.05)	13.22 (0.22)	12.16 (0.30)	2.57 (0.08)	1.09 (0.06)	0.22 (0.30)	95.42 (0.71)	Mg no. 69.9
AW-23 T (11)	51.91 (0.53)	2.57 (0.04)	19.62 (0.25)	5.41 (0.29)	0.20 (0.07)	2.52 (0.16)	7.46 (0.23)	6.37 (0.15)	3.32 (0.11)	0.62 (0.10)	90.83 (0.60)	Mg no. 45.4
AW-24B PT (11)	49.77 (0.63)	2.85 (0.05)	18.97 (0.23)	7.36 (0.25)	0.19 (0.06)	3.00 (0.15)	7.47 (0.14)	6.25 (0.12)	2.95 (0.07)	1.18 (0.10)	93.35 (0.89)	Mg no. 42.1
AW-25 PT (5)	48.80 (0.38)	2.85 (0.04)	18.80 (0.44)	9.23 (0.06)	0.23 (0.04)	2.95 (0.03)	7.59 (0.08)	5.87 (0.17)	2.80 (0.12)	0.88 (0.04)	95.45 (0.45)	Mg no. 36.3
AW-26 PT (6)	48.54 (0.38)	2.80 (0.06)	18.49 (0.17)	9.34 (0.21)	0.23 (0.06)	2.81 (0.07)	7.58 (0.10)	5.87 (0.09)	3.03 (0.05)	1.31 (0.03)	96.49 (0.52)	Mg no 34.9
AW-27 PT (27)	48.54 (0.36)	2.87 (0.03)	18.95 (0.44)	9.52 (0.24)	0.25 (0.03)	2.91 (0.04)	7.62 (0.05)	5.72 (0.35)	2.83 (0.12)	0.79 (0.04)	93.53 (0.66)	Mg no. 35.2
AW-29 PT (12)	48.44 (0.49)	3.10 (0.10)	18.03 (0.56)	8.26 (0.53)	0.25 (0.09)	3.10 (0.17)	7.72 (0.31)	6.49 (0.14)	3.35 (0.18)	1.25 (0.12)	94.84 (0.76)	Mg no. 40.1
plag (3)	51.84 (1.4)	1.37 (0.76)	24.80 (2.60)	4.14 (2.30)	0.10 (0.08)	1.07 (0.67)	9.72 (1.01)	4.83 (0.21)	1.40 (0.58)	n.d.	99.27 (0.61)	An$_{65}$Al$_{29}$Or$_6$
AW-33 PT (6)	49.07 (0.4)	2.61 (0.05)	18.41 (0.18)	8.63 (0.33)	0.24 (0.08)	2.74 (0.03)	7.70 (0.29)	6.18 (0.11)	3.19 (0.11)	1.20 (0.27)	94.66 (0.85)	Mg no. 36.2
AW-34 PT (6)	48.78 (0.79)	2.85 (0.05)	18.78 (0.15)	8.37 (0.29)	0.23 (0.05)	2.56 (0.08)	7.88 (0.09)	6.07 (0.12)	3.06 (0.05)	1.42 (0.08)	90.41 (1.05)	Mg no. 35.3
AW-37 PT (10)	48.39 (0.77)	3.02 (0.07)	18.64 (0.31)	8.76 (0.26)	0.25 (0.06)	2.95 (0.08)	7.69 (0.13)	5.94 (0.11)	3.05 (0.05)	1.30 (0.06)	96.86 (1.47)	Mg no. 37.5
AW-38 PT (6)	49.97 (0.51)	2.68 (0.07)	19.64 (0.21)	7.92 (0.13)	0.19 (0.07)	2.82 (0.03)	7.58 (0.12)	5.11 (0.26)	2.96 (0.06)	1.14 (0.06)	92.42 (0.98)	Mg no. 38.8
AW-39 PT (11)	51.30 (0.55)	2.40 (0.07)	19.95 (0.30)	6.49 (0.20)	0.19 (0.06)	2.70 (0.16)	7.47 (0.20)	5.65 (0.19)	3.12 (0.11)	0.71 (0.04)	94.25 (0.92)	Mg no. 42.6
AW-40 PT (11)	50.51 (0.62)	2.46 (0.07)	19.55 (0.28)	7.20 (0.11)	0.23 (0.05)	2.76 (0.10)	7.42 (0.17)	5.89 (0.11)	3.15 (0.06)	0.83 (0.06)	95.74 (1.23)	Mg no. 40.6
AW-41 T (12)	53.73 (0.82)	1.72 (0.05)	20.18 (0.38)	5.97 (0.14)	0.22 (0.06)	1.57 (0.07)	5.25 (0.14)	6.86 (0.14)	4.03 (0.08)	0.46 (0.03)	95.79 (1.40)	Mg no. 32.0
kaers (5)	38.19 (0.3)	6.08 (0.21)	13.61 (0.17)	11.44 (0.31)	0.24 (0.02)	11.45 (0.26)	11.79 (0.33)	2.73 (0.05)	1.14 (0.04)	n.d. (0.00)	96.66 (0.25)	Mg no. 64.1
AW-42 T (9)	52.77 (0.46)	1.63 (0.05)	20.30 (0.30)	6.16 (0.24)	0.23 (0.07)	1.94 (0.03)	4.25 (0.11)	7.37 (0.21)	4.68 (0.07)	0.67 (0.06)	97.88 (0.95)	Mg no. 35.9
kaers (2)	38.78 (0.8)	7.03 (0.36)	13.15 (0.12)	11.38 (0.35)	0.28 (0.05)	11.27 (0.09)	11.86 (0.40)	2.57 (0.08)	1.32 (0.04)	n.d.	97.63 (0.45)	Mg no. 63.8
plag (4)	55.57 (2)	0.69 (0.34)	25.75 (1.28)	1.42 (0.61)	0.05 (0.03)	0.28 (0.13)	9.15 (1.42)	5.96 (0.25)	1.14 (0.27)	n.d.	100.03 (1.58)	An$_{60}$Al$_{36}$Or$_4$
AW-43 PT (1)	52.00	2	21.12	5.96	0.22	1.21	4.95	7.62	4.05	0.86	98.55	Mg no. 27.0
cpx (4)	45.37 (0.66)	2.46 (0.50)	6.68 (1.09)	8.72 (0.40)	0.38 (0.02)	11.44 (0.46)	21.63 (0.71)	1.01 (0.12)	0.08 (0.01)	n.d.	97.77 (0.68)	En$_{36}$Wo$_{49}$Fe$_{15}$
plag (3)	56.35 (1)	0.91 (0.58)	24.12 (1.13)	2.58 (1.43)	0.08 (0.05)	0.84 (0.68)	7.97 (0.50)	5.36 (0.32)	1.87 (0.13)	n.d.	100.09 (0.65)	An$_{57}$Al$_{35}$Or$_8$
AW-44 T (11)	54.57 (0.8)	1.63 (0.05)	20.59 (0.32)	5.29 (0.13)	0.17 (0.06)	1.28 (0.06)	4.71 (0.12)	7.07 (0.16)	4.30 (0.08)	0.38 (0.04)	96.74 (1.46)	Mg no. 30.2
kaers (6)	38.20 (0.41)	5.92 (0.19)	13.58 (0.16)	12.34 (0.19)	0.28 (0.03)	11.92 (0.16)	11.44 (0.20)	2.75 (0.07)	1.27 (0.04)	0.21 (0.19)	97.93 (0.65)	Mg no. 63.3
AW-45 T (4)	53.03 (0.89)	1.91 (0.05)	20.69 (0.26)	5.55 (0.23)	0.21 (0.01)	1.68 (0.02)	6.34 (0.06)	6.95 (0.15)	3.37 (0.05)	0.26 (0.04)	92.94 (1.32)	Mg no. 35.1
kaers (5)	37.03 (0.83)	5.06 (0.26)	14.44 (0.20)	12.11 (0.71)	0.24 (0.01)	11.42 (0.43)	11.91 (0.55)	2.73 (0.15)	1.21 (0.11)	n.d.	96.18 (0.67)	Mg no. 62.7
AW-46 B-TA (9)	52.98 (0.87)	2.18 (0.09)	20.49 (0.67)	5.54 (0.39)	0.20 (0.08)	2.00 (0.21)	7.10 (0.40)	5.68 (0.29)	3.16 (0.19)	0.66 (0.21)	93.74 (1.86)	Mg no. 39.2
kaers (4)	38.54 (0.58)	4.58 (0.10)	14.07 (0.36)	10.64 (0.27)	0.21 (0.05)	13.28 (0.16)	12.23 (0.18)	2.66 (0.03)	1.15 (0.06)	n.d. (0.00)	97.41 (0.38)	Mg no. 69.0
AW-47 B-TA (10)	51.80 (0.2)	2.53 (0.04)	20.16 (0.26)	6.56 (0.12)	0.22 (0.07)	2.79 (0.07)	7.31 (0.07)	4.66 (0.23)	3.17 (0.07)	0.79 (0.05)	92.26 (0.43)	Mg no. 43.2

(continued)

Table 4: Continued

KI-04 basanite experiments

	Phase	SiO$_2$	TiO$_2$	Al$_2$O$_3$	FeO^T	MnO	MgO	CaO	Na$_2$O	K$_2$O	P$_2$O$_5$	Total	Mol %
KI-06	B (3)	45·92 (0·21)	4·37 (0·02)	14·42 (0·11)	10·22 (0·05)	0·25 (0·04)	7·81 (0·18)	13·03 (0·31)	3·35 (0·32)	0·64 (0·01)	n.d.	90·87 (0·03)	Mg no. 57·7
	ol (5)	40·67 (0·08)	0·09 (0·01)	0·03 (0·01)	9·41 (0·25)	0·25 (0·02)	49·09 (0·23)	0·35 (0·01)	0·01 (0·01)	0·01 (0·00)	n.d.	99·93 (0·13)	Fo$_{90}$
KI-07	B (15)	44·61 (0·38)	4·37 (0·09)	14·41 (0·20)	10·61 (0·40)	0·17 (0·04)	7·69 (0·19)	11·55 (0·25)	3·93 (0·11)	1·74 (0·13)	0·92 (0·04)	96·88 (0·63)	Mg no. 56·4
	ol (3)	38·33 (1·35)	0·65 (0·45)	0·50 (0·38)	14·11 (2·45)	0·22 (0·01)	45·11 (2·17)	0·49 (0·10)	0·10 (0·02)	0·03 (0·01)	n.d.	99·75 (1·09)	Fo$_{85}$
KI-08	B (16)	44·04 (0·49)	4·54 (0·13)	14·46 (0·44)	11·51 (0·61)	0·16 (0·05)	7·11 (1·31)	11·59 (0·46)	3·90 (0·14)	1·79 (0·08)	0·91 (0·05)	98·24 (0·79)	Mg no. 52·4
	ol (5)	39·56 (0·52)	0·21 (0·13)	0·12 (0·11)	12·93 (0·55)	0·27 (0·02)	46·09 (0·59)	0·40 (0·03)	0·02 (0·01)	0·01 (0·00)	n.d.	99·63 (0·22)	Fo$_{86}$
KI-09	PT (9)	49·66 (0·37)	2·87 (0·06)	18·78 (0·37)	7·01 (0·38)	0·14 (0·05)	3·13 (0·09)	6·42 (0·14)	7·01 (0·14)	3·76 (0·08)	1·22 (0·11)	94·67 (0·72)	Mg no. 44·3
	cpx (4)	44·34 (0·82)	3·44 (0·37)	8·29 (1·03)	7·82 (0·57)	0·12 (0·04)	12·35 (0·76)	20·82 (0·73)	0·65 (0·08)	0·18 (0·12)	n.d.	98·06 (0·18)	En$_{39}$Wo$_{47}$Fe$_{14}$
KI-10	B (8)	47·27 (0·79)	3·65 (0·26)	16·32 (1·20)	7·96 (0·38)	0·20 (0·08)	5·89 (1·61)	9·28 (1·34)	5·44 (0·57)	2·60 (0·32)	1·39 (0·23)	92·05 (1·04)	Mg no. 56·9
	ol (3)	38·82 (0·18)	0·19 (0·07)	0·17 (0·14)	17·98 (0·40)	0·33 (0·01)	41·25 (0·49)	0·71 (0·28)	0·02 (0·00)	0·02 (0·00)	n.d.	99·51 (0·22)	Fo$_{80}$
KI-11	cpx (5)	43·08 (0·46)	4·38 (0·22)	9·98 (0·31)	8·46 (0·43)	0·12 (0·03)	11·14 (0·21)	20·96 (0·33)	0·82 (0·09)	0·18 (0·05)	n.d.	99·23 (0·45)	En$_{36}$Wo$_{49}$Fe$_{15}$
	B (5)	47·87 (0·26)	3·78 (0·06)	16·71 (0·24)	8·25 (0·22)	0·20 (0·07)	4·86 (0·20)	9·18 (0·09)	5·35 (0·22)	2·34 (0·13)	1·47 (0·09)	92·99 (0·25)	Mg no. 51·2
KI-12	kaers (5)	37·68 (1·47)	5·75 (0·38)	12·08 (0·15)	11·79 (2·45)	0·11 (0·03)	15·25 (0·31)	11·66 (0·70)	2·51 (0·07)	1·07 (0·06)	n.d.	97·97 (1·22)	Mg no. 70·0
	B (11)	45·59 (0·48)	4·54 (0·08)	16·01 (0·15)	8·54 (0·30)	0·16 (0·11)	5·89 (0·34)	11·32 (0·38)	4·88 (0·13)	1·90 (0·20)	1·17 (0·11)	91·56 (0·98)	Mg no. 55·2
	ol (7)	38·65 (0·32)	0·14 (0·04)	0·09 (0·06)	11·64 (0·16)	0·25 (0·03)	47·16 (0·50)	0·43 (0·23)	0·05 (0·02)	0·01 (0·01)	n.d.	98·48 (0·36)	Fo$_{88}$
KI-14	cpx (4)	44·23 (0·98)	3·05 (0·28)	5·92 (0·47)	6·95 (0·49)	0·12 (0·01)	14·45 (0·48)	22·75 (0·14)	0·65 (0·12)	0·07 (0·01)	n.d.	98·26 (0·52)	En$_{42}$Wo$_{47}$Fe$_{11}$
	B (7)	44·62 (0·39)	5·11 (0·06)	15·75 (0·28)	10·25 (0·44)	0·21 (0·13)	5·58 (0·17)	10·56 (0·14)	4·68 (0·13)	2·20 (0·12)	1·03 (0·09)	96·57 (1·00)	Mg no. 49·3
	ol (4)	38·05 (0·16)	0·16 (0·02)	0·09 (0·06)	20·19 (0·31)	0·32 (0·05)	40·21 (0·47)	0·53 (0·13)	0·05 (0·04)	0·03 (0·01)	n.d.	99·71 (0·26)	Fo$_{78}$
KI-15	B (15)	43·55 (0·37)	4·94 (0·08)	14·37 (0·24)	11·28 (0·32)	0·19 (0·06)	6·73 (0·22)	12·11 (0·28)	4·06 (0·12)	1·81 (0·14)	0·97 (0·09)	93·70 (0·69)	Mg no. 51·5
	ol (8)	38·72 (0·13)	0·11 (0·02)	0·04 (0·02)	16·69 (0·14)	0·26 (0·06)	42·84 (0·27)	0·41 (0·02)	0·01 (0·01)	0·01 (0·01)	n.d.	99·17 (0·29)	Fo$_{82}$
KI-16	B (15)	43·81 (0·30)	4·83 (0·09)	14·35 (0·23)	11·52 (0·23)	0·19 (0·12)	6·73 (0·30)	12·20 (0·48)	4·03 (0·12)	1·40 (0·20)	0·95 (0·08)	94·20 (0·59)	Mg no. 51·0
	ol (8)	39·25 (0·27)	0·13 (0·03)	0·07 (0·03)	15·27 (0·08)	0·26 (0·03)	43·90 (0·23)	0·40 (0·03)	0·07 (0·02)	0·02 (0·01)	n.d.	99·42 (0·21)	Fo$_{84}$
KI-17	B (1)	44·80	4·43	14·88	11·17	0·2	6·68	11·66	3·84	1·73	0·57	95·16	Mg no. 51·6
KI-20	ol (4)	39·42 (0·52)	0·11 (0·02)	0·05 (0·02)	13·51 (0·29)	0·24 (0·03)	45·76 (0·27)	0·33 (0·01)	0·02 (0·02)	0·00 (0·01)	n.d.	99·58 (0·92)	Fo$_{86}$
	B (5)	45·05 (0·41)	4·44 (0·10)	14·40 (0·11)	11·23 (0·17)	0·21 (0·02)	7·74 (0·60)	12·31 (0·88)	3·11 (0·34)	0·91 (0·27)	0·60 (0·04)	92·55 (0·61)	Mg no. 55·1
KI-21	B (8)	43·60 (0·36)	4·69 (0·07)	14·17 (0·09)	11·77 (0·23)	0·15 (0·04)	8·03 (0·09)	11·38 (0·19)	3·62 (0·05)	1·66 (0·11)	0·93 (0·07)	95·28 (0·69)	Mg no. 54·9
	ol (4)	39·00 (0·44)	0·12 (0·03)	0·05 (0·03)	14·38 (0·33)	0·23 (0·02)	46·75 (0·97)	0·34 (0·03)	0·02 (0·02)	0·00 (0·01)	n.d.	101·01 (0·68)	Fo$_{85}$
KI-22	B (10)	43·42 (0·43)	4·74 (0·10)	14·46 (0·21)	11·71 (0·34)	0·20 (0·05)	7·32 (0·25)	11·60 (0·13)	3·81 (0·09)	1·82 (0·06)	0·92 (0·06)	96·02 (1·19)	Mg no. 52·7
	ol (8)	39·07 (0·45)	0·12 (0·09)	0·13 (0·23)	15·90 (0·83)	0·26 (0·04)	45·24 (0·97)	0·52 (0·46)	0·03 (0·03)	0·01 (0·01)	n.d.	101·36 (0·72)	Fo$_{83}$
KI-23	B (10)	43·63 (0·61)	4·95 (0·08)	15·04 (0·30)	11·26 (0·31)	0·19 (0·05)	6·49 (0·12)	11·49 (0·12)	4·11 (0·07)	1·88 (0·04)	0·96 (0·03)	97·21 (1·30)	Mg no. 50·7
	ol (5)	38·71 (0·37)	0·13 (0·01)	0·05 (0·01)	18·74 (0·19)	0·26 (0·04)	43·25 (0·23)	0·51 (0·01)	0·01 (0·01)	0·01 (0·01)	n.d.	101·74 (0·69)	Fo$_{80}$
	cpx (6)	43·57 (1·60)	4·44 (0·54)	11·33 (1·99)	8·29 (1·21)	0·17 (0·01)	9·82 (1·89)	17·67 (2·74)	1·60 (0·78)	0·79 (0·48)	n.d.	97·96 (1·25)	En$_{36}$Wo$_{47}$Fe$_{17}$
KI-26	B (6)	43·76 (0·58)	4·48 (0·11)	13·75 (0·19)	11·45 (0·49)	0·16 (0·07)	9·33 (1·38)	11·04 (1·59)	3·49 (0·17)	1·64 (0·68)	0·90 (0·04)	96·65 (0·35)	Mg no. 59·2
KI-27	B (6)	43·48 (0·63)	4·48 (0·04)	14·63 (0·21)	10·79 (0·17)	0·15 (0·05)	9·06 (1·15)	11·74 (0·11)	4·09 (0·09)	1·57 (0·15)	n.d.	92·24 (0·82)	Mg no. 59·9
KI-28	B (6)	44·61 (0·41)	4·55 (0·05)	14·25 (0·16)	9·89 (0·11)	0·21 (0·04)	8·98 (0·07)	11·40 (0·08)	3·76 (0·12)	1·69 (0·11)	0·66 (0·02)	95·99 (0·33)	Mg no. 61·8
KI-31	PT (3)	51·87 (0·66)	2·68 (0·16)	18·59 (0·33)	8·22 (0·31)	0·23 (0·05)	2·98 (0·08)	7·70 (0·05)	5·19 (0·13)	2·55 (0·01)	n.d.	92·06 (0·66)	Mg no. 39·2
	kaers (8)	39·82 (0·73)	4·88 (0·17)	11·94 (0·49)	11·05 (0·45)	0·15 (0·05)	14·04 (0·40)	11·58 (0·14)	2·64 (0·06)	1·21 (0·05)	0·09 (0·10)	97·49 (0·44)	Mg no. 69·4
KI-32	PT (7)	49·92 (0·75)	3·22 (0·30)	17·06 (0·57)	8·94 (0·53)	0·23 (0·01)	4·43 (1·30)	9·14 (0·41)	4·19 (0·36)	2·18 (0·20)	0·69 (0·09)	91·46 (1·71)	Mg no. 46·9
	kaers (6)	39·67 (0·78)	4·04 (0·19)	11·91 (0·42)	10·45 (1·33)	0·18 (0·02)	14·94 (1·24)	11·84 (0·12)	2·58 (0·07)	1·24 (0·13)	0·15 (0·17)	97·09 (0·50)	Mg no. 71·7
KI-33	TB (7)	47·39 (0·70)	3·69 (0·06)	16·09 (0·02)	9·81 (0·32)	0·18 (0·05)	5·57 (0·27)	9·99 (0·15)	3·83 (0·14)	2·18 (0·09)	1·26 (0·06)	89·81 (1·41)	Mg no. 50·3
	kaers (4)	39·82 (0·82)	4·38 (0·07)	11·80 (0·56)	10·59 (0·35)	0·14 (0·04)	14·79 (0·31)	11·77 (0·27)	2·60 (0·05)	1·25 (0·05)	0·12 (0·19)	97·37 (0·20)	Mg no. 71·3
KI-36	B (10)	43·75 (0·61)	4·70 (0·08)	14·24 (0·28)	11·33 (0·27)	0·18 (0·08)	8·21 (0·31)	11·46 (0·35)	3·56 (0·10)	1·66 (0·11)	0·91 (0·07)	94·04 (1·40)	Mg no. 56·4
	ol (13)	39·22 (0·21)	0·09 (0·02)	0·04 (0·01)	15·30 (0·35)	0·24 (0·03)	45·80 (0·28)	0·33 (0·02)	0·02 (0·01)	0·01 (0·01)	n.d.	101·17 (0·57)	Fo$_{84}$
KI-37	ol (10)	39·72 (0·35)	0·09 (0·02)	0·04 (0·01)	14·17 (0·43)	0·22 (0·04)	46·99 (0·41)	0·28 (0·02)	0·01 (0·01)	0·01 (0·01)	n.d.	101·70 (0·66)	Fo$_{86}$

Analyses given in wt % and normalized to 100% with original analysis total given. Numbers in parentheses next to analyses are standard deviations; those next to phase names are number of analyses. n.d., not determined. Reported values for glasses are average compositions for each charge. FeO^T, total iron given as FeO. Glass name classifications: B, basanite; PT, phonotephrite; T, tephriphonolite; P, phonolite; B-TA, basaltic trachyandesite; TB, trachybasalt. Mg no. calculated as molar MgO/(FeO^T + MgO).
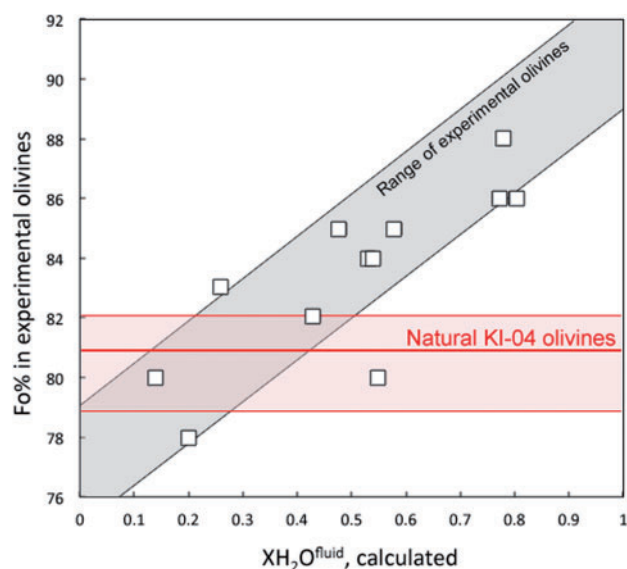
Fig. 6. Chemical compositions of experimental olivines in terms of Fo content versus the calculated equilibrium $X\mathrm{H_2O^{fluid}}$, illustrating a general positive correlation between the two variables. The Fo content of natural KI-04 olivines is indicated by the horizontal red line. The gray shaded region represents the average range of experimental Fo contents in olivines and respective $X\mathrm{H_2O^{fluid}}$ values. The intersection of this region with the red line thus indicates the range of expected $X\mathrm{H_2O^{fluid}}$ values for the natural KI-04 magma based solely on olivine composition at the investigated pressures (200–400 MPa).

saturated in Cpx ± OI and kaersutite define a common general and relatively narrow trend in such a diagram, despite the compositional differences existing between the three bulk-rock compositions used to establish the cotectics. Significant departure of a Cpx ± OI-bearing mafic rock composition from this trend might indicate that accumulation or contamination processes of some sort have occurred.

AW-related charges produced liquids compositionally different from the starting material mostly at 1000°C. Liquids produced at higher temperatures cluster broadly around the bulk-rock AW composition. As observed for KI, two distinct trends appear depending on whether kaersutite or Cpx ± Pl is the dominant fractionating silicate. In both cases, the most evolved compositions reach the phonolitic field with SiO_2 in excess of 52–53 wt %. Kaersutite-saturated liquids in particular have higher MgO and CaO contents, whereas liquids crystallizing Cpx ± Pl have higher K_2O (at the same SiO_2 content). For most major elements in AW experiments, there is no apparent effect of pressure, liquid compositions being governed mostly by variations in T and H_2O. The sole exception is Al_2O_3: liquids produced at 400 MPa are distinctly richer in Al_2O_3 relative to those at 200 MPa, the former having >20 wt % Al_2O_3 whereas at 200 MPa the majority of liquids have less than 20 wt %. This reflects in part the fact that, for the AW composition, kaersutite crystallization depletes the liquid less in Al_2O_3 relative to Cpx and Pl.

DISCUSSION

Pre-eruptive conditions of KI and AW magmas and the production of the phonolite lava lake

Overall, the experimental mineral phases reproduce those observed in the natural rocks, showing that our experiments correctly capture the natural system in terms of fO_2–T–H_2O conditions of evolution. In detail, experiments best reproducing the OI composition of KI (Fo_{78-80}) are at around 1100°C and with less than 1·5 wt % dissolved H_2O (corresponding to $X\mathrm{H_2O^{fluid}} < 0·2$; charges KI-10, KI-14 and KI-23, Table 4), in the pressure range 200–300 MPa. Higher melt water contents would yield olivine that is too magnesian. The natural DVDP clinopyroxene composition was best reproduced at 200 MPa and 1050°C as shown in Fig. 10 (sample KI-12; $En_{42}Wo_{47}Fs_{11}$). Other experimental pyroxenes are more iron-rich (Fs_{14-17}) than those in the natural samples, although the most Fe-rich clinopyroxenes measured (KI-23) are possibly quench crystals, as indicated by high variability in Ca and Na, and high K. It should be noted that the experimental clinopyroxenes are in general rich in Al_2O_3 and Na_2O, consistent with those in the natural rocks (Kyle, 1981). This Al- and Na-rich character of Cpx does not therefore reflect crystallization at higher pressure (e.g. Kyle, 1981) but instead the Al- and Na-rich character of the melt from which the pyroxenes grew. Experiments between NNO + 1·5 and NNO + 2 produced kaersutite that most closely resembles the natural amphiboles in terms of Ti content ($\sim$5·5–6·5 wt % TiO_2) and average Mg# (65), although the natural amphiboles have a significant spread in Mg# (56–72) (Fig. 11). Most natural DVDP amphiboles contain 12·5–14 wt % Al_2O_3 (Kyle, 1981), resembling the compositional range of experimental AW amphiboles. Given the correlation between kaersutite Al contents and pressure (Fig. 12), this suggests that significant DVDP differentiation [in which the role of amphibole is important (Kyle, 1981)] occurred at 200–400 MPa. The An contents in experimental phonotephrite feldspars range from An_{57} to An_{65} and closely mimic the compositions of natural phonotephrite feldspars (Fig. 13). The fact that the Or contents of experimental plagioclases are higher than those of the natural rocks is probably due to contamination of the microprobe analyses by surrounding glass.

The experiments allow us to constrain possible petrogenetic paths for magma production at Erebus. We first consider the production of intermediate, AW-like, magmas from a KI-type parent. To this end, the AW bulk-rock has been plotted in Fig. 8 displaying KI-related liquids. As can be seen here, an AW-type liquid (48 wt % SiO_2) is bracketed for several oxides by charges run at 1050°C and 200 MPa (between KI-09 and KI-10), in particular for Na_2O, K_2O and CaO, and to a lesser extent Al_2O_3 and TiO_2. FeO, which is too low in the experiments (8 wt % vs 9·4 wt %), does not fit these trends, suggesting therefore that the experimental fO_2 is slightly too oxidized compared with nature. The
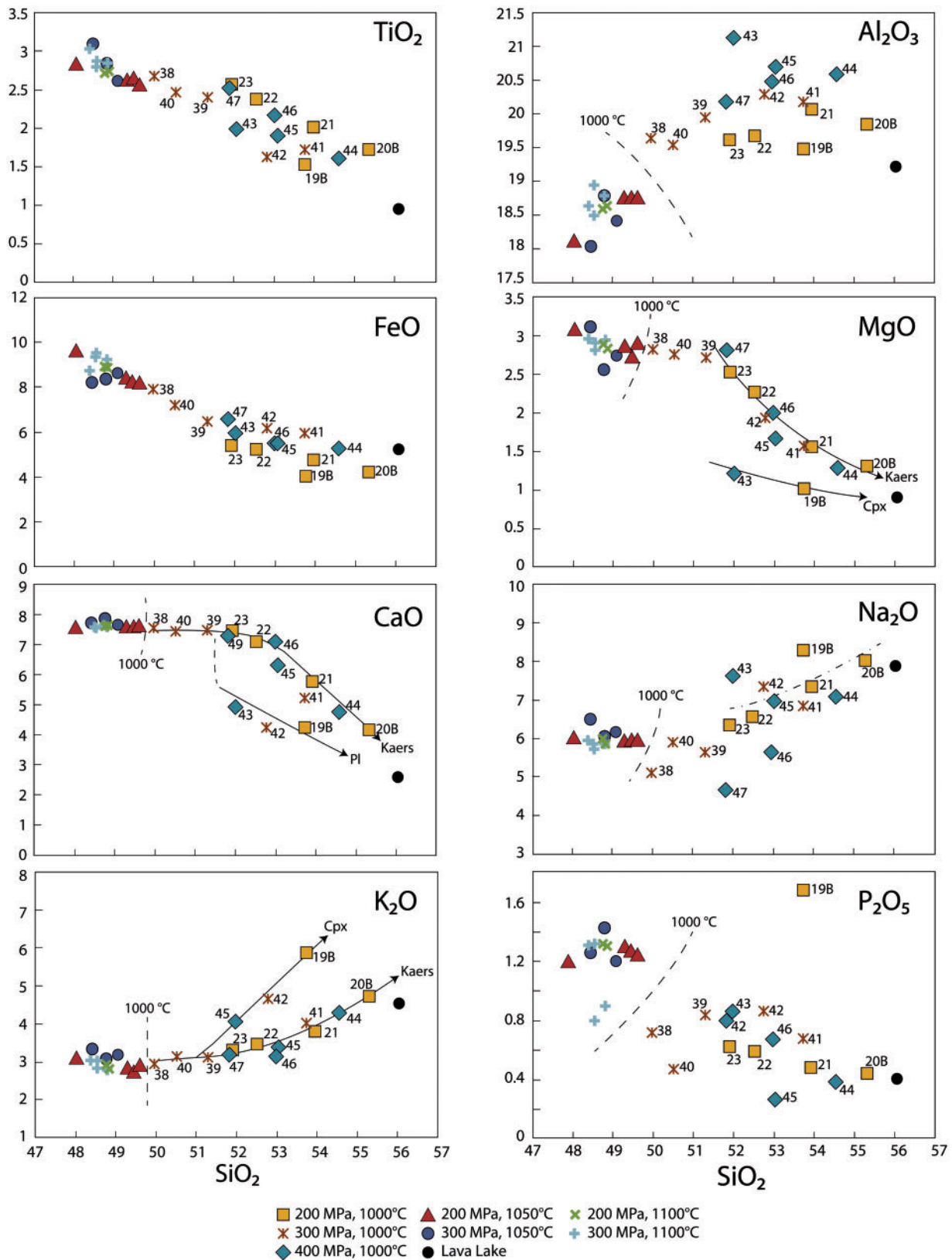
Fig. 7. Harker variation diagrams for AW experimental glasses illustrating the production of a phonolite magma resembling that in the Erebus lava lake [the composition used by Moussallam *et al.* (2013); black dot] by crystallization of an AW-type magma. The liquids that best approximate the lava lake composition are the driest ones at 1000°C (<1·7 wt %) for all pressures. The closest experimental analogues are charges AW-19B and AW-20B at 200 MPa. Lower than natural FeO concentrations in these two runs could indicate that the experiments were too oxidized relative to the natural magmas. High experimental CaO contents may indicate that the production of lava lake phonolite requires lower temperatures, possibly around 975°C. The roles of kaersutite and Cpx ± Pl crystallization are clearly defined by two distinct evolutionary trends.
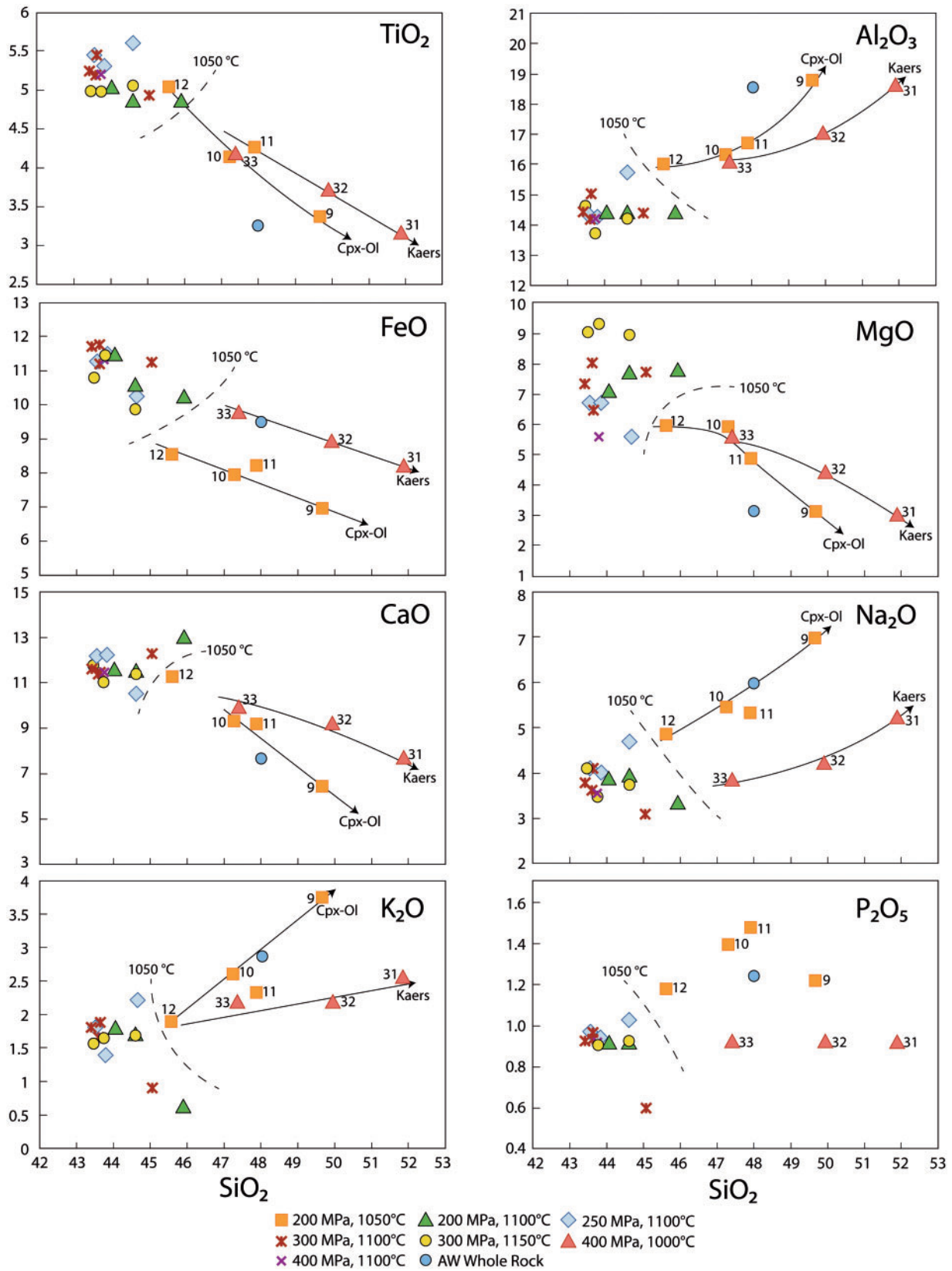
Fig. 8. Harker variation diagrams for KI experimental glasses illustrating the production of intermediate AW-like magmas (represented here by the AW whole-rock; blue dot) from a KI-type parent. At low *T*, two evolutionary trends are apparent in which either Cpx ± Pl or kaersutite amphibole is the dominant fractionating phase. An AW-type daughter liquid is bracketed for several oxides by experiments KI-09 and KI-10, thus constraining the melt water content reached at the stage of AW magma production to between 0·7 and 1·5 wt %. FeO is too low in the experimental charges relative to natural AW whole-rocks, indicating that the experiments were more oxidized than the natural magmas.
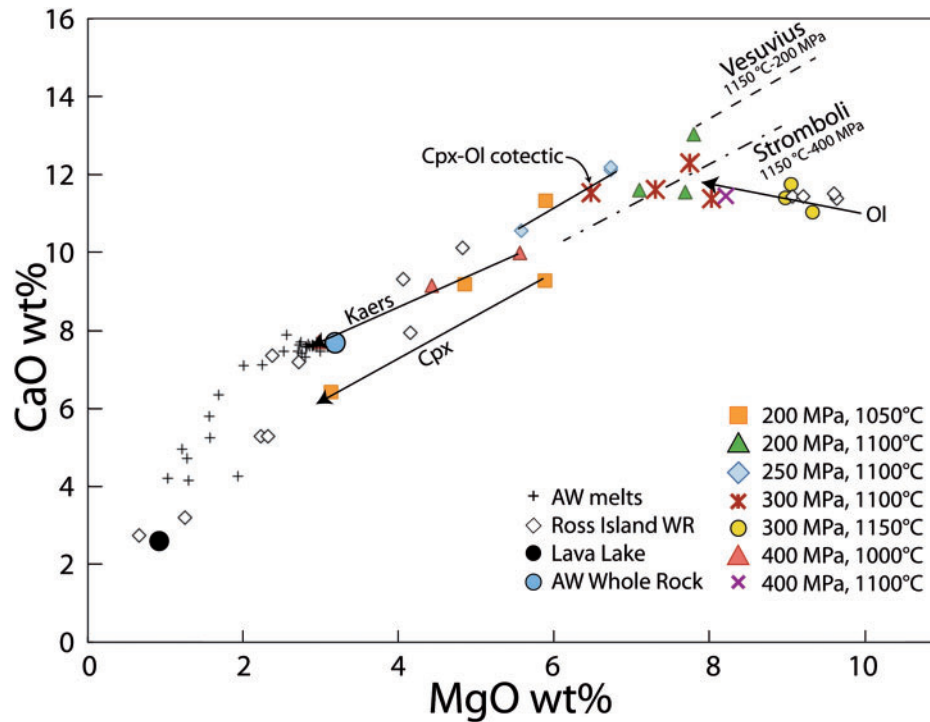
Fig. 9. CaO vs MgO plot showing the compositions of cotectic and near-cotectic experimental glasses, which mimic natural whole-rock compositions from a suite of Ross Island lavas (open diamonds), useful in identifying trends in compositions dominated by the precipitation of olivine and Ca-pyroxene (or amphibole). KI runs are shown with different symbols in terms of *P–T* conditions. The Cpx–Ol cotectic at 1050°C is shown for KI melts. Also plotted are experimentally determined Cpx–Ol cotectics for melts from Stromboli (Pichavant *et al.*, 2009) and Vesuvius (Pichavant *et al.*, 2014). Despite compositional differences in the starting materials used in these three studies, mafic alkali-rich liquids saturated in Cpx ± Ol and kaersutite define a relatively narrow evolutionary trend in this diagram. KI melts are marked by initial Ol crystallization, followed by either Cpx ± Pl or Kaers.
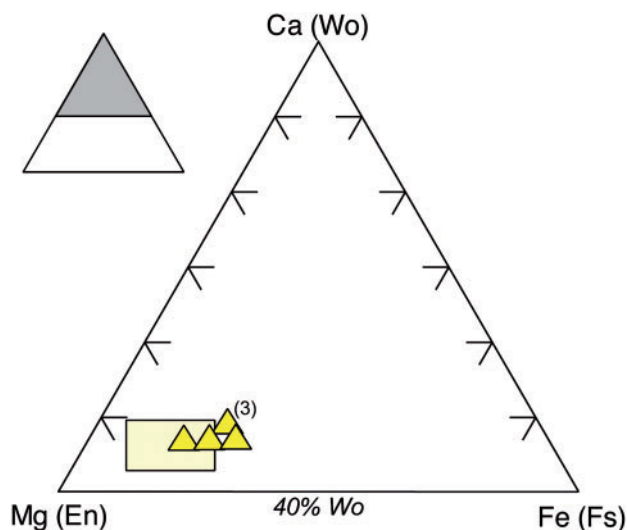
Fig. 10. Enlarged ternary diagram (from 40% Wo) showing the compositions of experimental (symbols) and natural (yellow box) clinopyroxenes, plotted in terms of recalculated end-member compositions enstatite, ferrosilite and wollastonite. The number (3) indicates three samples with the same composition.

corresponding melt water content reached at the stage of AW magma production is thus bracketed by that of those two charges, between 0·7 and 1·5 wt % (Table 2).

We next evaluate the conditions for the production of a phonolite magma similar to that of the lava lake by crystallization of an AW-type magma (Fig. 7). The experimental AW liquids define a trend toward the lava lake composition [taken as the composition used by Moussallam *et al.* (2013)], although that end-member is not bracketed by the experimental results. At all pressures, the liquids best approaching the lava lake are the driest ones at 1000°C (<1·7 wt %). In detail, the liquids obtained at 400 MPa are too Al_2O_3-rich relative to that of the lava lake, suggesting this is too high a pressure for phonolite production in the Erebus plumbing system. In contrast, the two driest liquids at 200 MPa (AW-19B and AW-20B) are close synthetic analogues for the lava lake, charge AW-19B having the observed mineralogy of the lava lake. Notably, the TiO_2 trend falls short, with experimental liquids being 0·5 wt % too rich in TiO_2 relative to the lava lake, suggesting a lower temperature for the natural system. FeO concentrations in those two driest 200 MPa charges are slightly below that of the lava lake, which could be taken to indicate that the experimental fO_2 is slightly too high, as inferred above for the production of AW magmas. The MgO and CaO trends clearly distinguish the role of kaersutite versus that of Cpx ± Pl, suggesting again the latter assemblage as the dominant one during differentiation of the EL. It is in CaO content that the difference between the
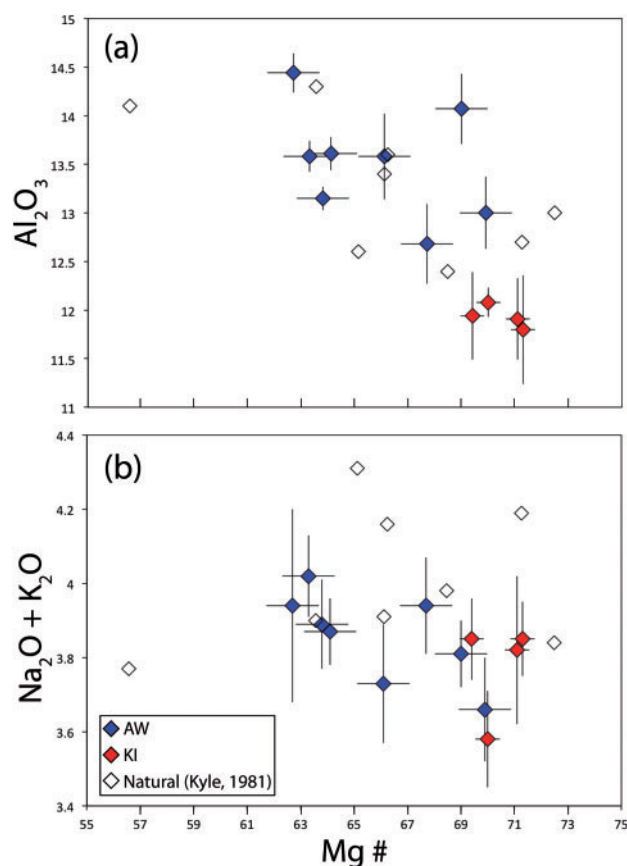
Fig. 11. Chemical compositions of experimental (filled diamonds) and natural (open diamonds) kaersutite amphibole, plotted in terms of magnesium number versus Al_2O_3 (a) and $Na + K$ (a). Natural kaersutites are from intermediate and evolved DVDP lavas from Kyle (1981). Error bars represent 1SD.

Fig. 12. Compositions of experimental AW kaersutite illustrating the positive correlation between pressure and Al_2O_3 content. The majority of natural DVDP amphiboles have 12·5–14 wt % Al_2O_3 (grey box), suggesting that significant fractionation of DVDP magmas took place between 200 and 400 MPa. Vertical error bars represent 1SD. Horizontal error bars (±20 bar) are smaller than symbols.
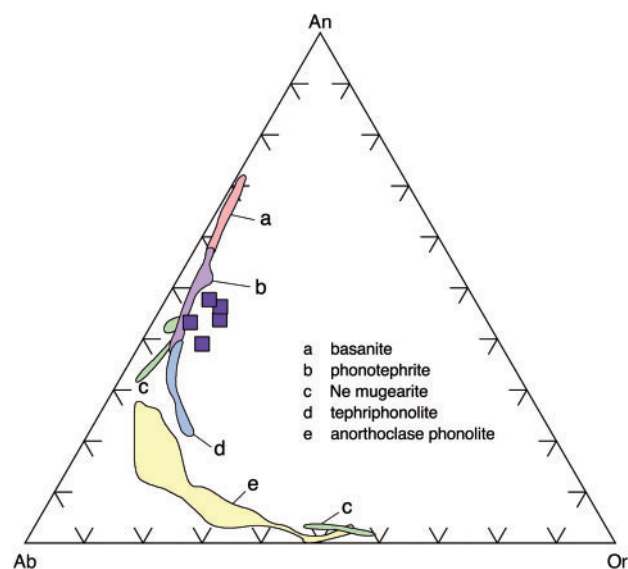
Fig. 13. Ternary diagram showing the compositions of experimental plagioclase (purple squares) and natural plagioclase from EL lavas [shaded fields; data from Kyle *et al*. (1992)]. It should be noted that all experimental plagioclase crystals were very small and so their chemical analyses via EMP may be contaminated by the surrounding glass.

experimental liquids and the lava lake is greatest. Inspection of the experimental CaO trends suggests that the production of a magma with a CaO content similar to that of the lava lake requires temperatures below 1000°C, possibly around 975°C. This is in agreement with the work of Moussallam *et al.* (2013), who experimentally determined the liquidus of the phonolite lava lake under nearly dry conditions at 975–1000°C.

In summary, KI near-liquidus conditions are inferred to be around 1100°C and 1 ± 0.5 wt % H_2O at 200–300 MPa. Production of intermediate magmas at Erebus (AW-type) from a KI-type parent requires a temperature drop to around 1050°C at a pressure of 200 MPa, reaching slightly higher melt water contents but still below 1·5 wt %. Redox conditions appear to be moderately oxidized at this stage, possibly between those defined by the quartz–fayalite–magnetite (QFM) and NNO solid buffers, or just slightly above NNO. AW-type magma may in turn crystallize down to 975–1000°C, possibly in the pressure range 100–200 MPa, yielding a phonolitic liquid similar to that sustaining the lava lake, which is characterized by very low water contents and reduced conditions. As shown by Moussallam *et al.* (2014), the

transition between moderately oxidized conditions in the crustal magma reservoir and the more reduced conditions typifying the lava lake may result from degassing processes involving melt–COHS fluid equilibrium (see below). Although the temperature of the lava lake has been inferred to lie somewhere between 950 and 1080°C (see Introduction), the present study, in combination with that of Moussallam *et al* (2013), consistently favors the lower bound of that temperature range.

Differences between EL and DVDP magmatic evolution

Although neither experimental series completely reproduced the phase assemblages of the natural Erebus starting lavas (i.e. occurrence of kaersutite in EL experiments whereas it is not present in the corresponding rocks), our results shed light on critical aspects of the Erebus system and elucidate key differences in the formation conditions of the two natural lava suites. Plagioclase is confined to very low H_2O–high CO_2 conditions, suggesting maximum melt H_2O concentrations of ∼1–2 wt % for both EL and DVDP lava suites at the P–T conditions explored, consistent with melt inclusion volatile contents (Oppenheimer et al., 2011). The presence of kaersutite in all except the most primitive natural DVDP lavas suggests higher water activities for the DVDP suite compared with the EL, with $X H_2O^{fluid}$ around 0·2, indicated by the co-precipitation of plagioclase and kaersutite in phonotephrite experiments. The peritectic-like relationship inferred between olivine ($\pm$ clinopyroxene) and kaersutite allows us to place constraints on the relative temperatures of the EL and DVDP suites. All EL lavas plus DVDP basanites (the most primitive of which probably represents the parent melt for both suites) contain olivine and lack kaersutite. Conversely, all other DVDP lavas lack olivine and contain kaersutite. This is consistent with EL and primitive DVDP lavas being thermally buffered during the early and intermediate stages of differentiation to above 1050°C, with intermediate and evolved DVDP lavas undergoing a drop in equilibration temperature to below 1050°C.

The chemical compositions of both experimental series (squares and diamonds) and natural EL melt inclusions (shaded fields) are shown in variation diagrams of their major oxides versus SiO_2 in Fig. 14. Because of the rarity of melt pools large enough to be measured in the DVDP lavas, no residual melt compositions exist in the literature.

Many of the experimental glass compositions match the natural trends fairly well, but some are clearly offset, indicating a difference in natural versus experimental P–T–H_2O–fO_2 conditions for those charges.

Mismatch between natural and experimental glass compositions is notable in particular for CaO and MgO, and to a lesser extent for Al_2O_3. Higher than observed CaO values suggest insufficient fractionation of plagioclase and/or calcic clinopyroxene in the experiments compared with the natural lavas. The lack of plagioclase in the KI experiments and moderate plagioclase crystallization in the AW experiments may indicate that the liquid line of descent we have established experimentally is either hotter or, more probably, wetter than that of the natural system. Deep and intermediate magmas are not expected to be significantly cooler than the temperature of the surficial lava lake, which provides a thermal lower bound of ∼975–1000°C (Kyle, 1977; Caldwell & Kyle, 1994; Dunbar et al., 1994; Moussallam et al., 2013). It is

thus unlikely that significantly lower temperatures are responsible for enhanced calcic plagioclase crystallization in natural samples. For this reason, we suggest that the Ross Island magmas differentiated under lower water activities in our experiments, significantly constraining the natural $X H_2O^{fluid}$ conditions of the DVDP and EL series to \ll 0·25. The elevated MgO contents in the KI experiments relative to natural melt inclusions may reflect the lack of a cardinal phase consuming this element, in particular olivine, which in turn could be controlled by oxygen fugacity. Low experimental Al_2O_3 contents in KI melts may reflect insufficient plagioclase crystallization in addition to illustrating the dominant role of kaersutite fractionation in the DVDP magmas compared with EL melts, whose evolution is defined instead by Cpx fractionation.

Trends in the K_2O and P_2O_5 contents of natural EL glasses are distinct from those of EL and DVDP whole-rocks (Figs 2 and 14). Experimental K_2O melt contents mimic those of the whole-rock samples in that they are depleted relative to EL melt inclusions, probably reflecting the dominant role of kaersutite in our experiments and in natural DVDP rocks. The trends in P_2O_5 content illustrate well the onset of apatite saturation in experimental charges and natural EL melt inclusions. In EL lavas, apatite saturation occurs when the melts have differentiated such that the silica content is $\geq$48–49 wt %, after which P_2O_5 decreases with increasing SiO_2 (Fig. 14g), in agreement with existing solubility models (Harrison & Watson, 1984). This suggests a hotter temperature of c. >1100°C for the primitive and intermediate EL magmas, and a lower temperature (indicated by the onset of apatite saturation) for the evolved lavas.

Redox constraints on Ross Island magmatism

The presence of kaersutite in our experimental samples is largely independent of H_2O content. The growth of amphibole in relatively dry experiments indicates that some other component is taking the place of OH^- in the crystal structure. The role of fluorine is usually invoked to explain the enhanced stability of amphibole, but this has not been detected in the kaersutite of the DVDP rocks (Kyle, 1981). Unusually low H contents have been measured in other natural kaersutites (notably those from Martian meteorites) suggesting that the amphibole does not require a hydrous environment to grow (Popp & Phillips, 1995) In addition to Cl^- and F^- occupying O3 site occupancies, oxy substitutions in kaersutite are favored by high Ti and Fe^{3+} contents (Popp & Taras Bryndzia, 1992) via the reactions

$$Fe^{2+} + OH^- = Fe^{3+} + O^{2-} \qquad (4)$$

$$[6]Al^{3+} + OH^- = Ti^{4+} + O^{2-}. \qquad (5)$$
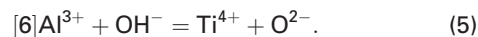
This may explain the growth of kaersutite in our driest experiments, especially given the oxidizing experimental conditions, which will favor oxy substitutions via the reaction in equation (4). The presence of kaersutite in
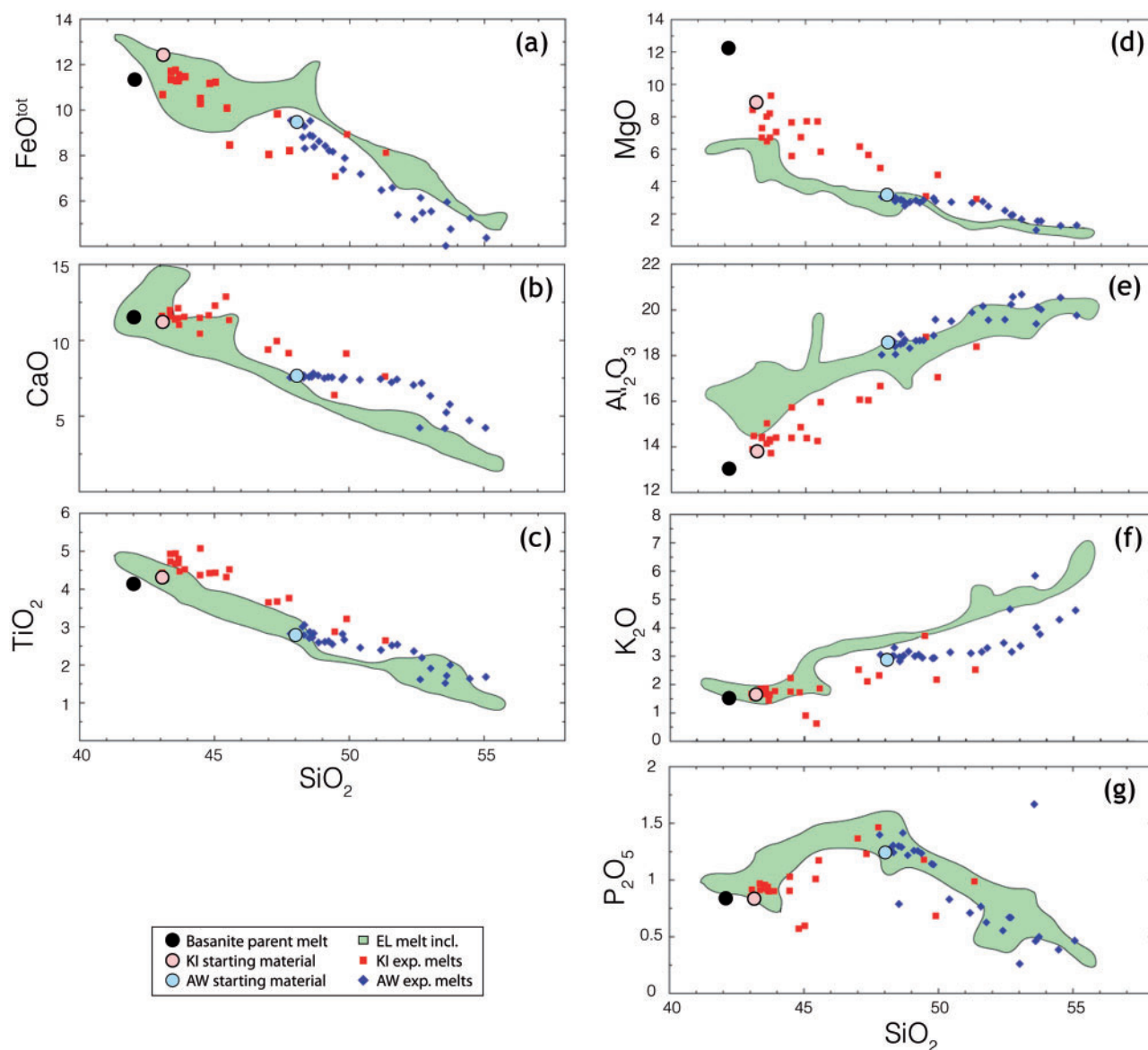
Fig. 14. Harker variation diagrams showing the compositions of experimental residual glasses (KI-04, red squares; AW-82038, blue diamonds) compared with compositions of olivine-hosted melt inclusions in EL lavas [green fields; data from Oppenheimer *et al.* (2011)]. The parent basanite composition is shown as a black dot, and compositions of starting materials used in this study are shown as pale red (basanite KI-04) and pale blue (phonotephrite AW-82038) dots.

relatively dry natural samples thus may indicate the prevalence of oxidizing conditions for the DVDP lavas.

Given that the natural phase assemblages were reproduced under the relatively oxidizing experimental conditions employed, we infer a similarly oxidizing environment for the deep and intermediate Ross Island magmas. This is in direct contrast to the reducing conditions (QFM – 1·22) inferred for Erebus's phonolitic lava lake (based on oxide pairs; Kyle, 1977) but is consistent with a reducing upwards redox trend that can be inferred for the EL. Based on the experimental study of Moussallam *et al.* (2013), a phonolite reservoir at 200 MPa has an oxygen fugacity of QFM – 0·5 at 1000°C. Intermediate tephriphonolites at 300 MPa have an estimated oxygen fugacity of QFM – 0·44 at 1081°C [based on oxide pairs from sample 97009 from Kyle *et al.* (1992)]. Coupled chemical–physical modeling of conduit flow by Burgisser & Scaillet (2007) has shown that reducing upwards behavior is expected for some sulfur-bearing volcanic systems. This is confirmed by the systematic analyses of the Fe redox state of a suite of melt inclusions at Erebus, which have conclusively shown a strong reduction trend as pressure decreases (Moussallam *et al.*, 2014). In addition, the large CO_2 flux proposed as the mechanism for dehydrating Erebus magmas might also contribute to the reduction in oxidation state of the shallow Erebus system by reducing H_2O fugacity.

The case for CO_2-dominated volcanism at Erebus

The results of this study add to the compelling evidence that Erebus volcano is a remarkably CO_2-rich, H_2O-poor system. Melt inclusion volatile contents from Erebus maintain markedly high C/H ratios, even in intermediate and evolved melts. Conceptually, this can be explained by the presence of a CO_2-rich gas buffering the melt to higher dissolved CO_2 concentrations, an interpretation consistent with previous modeling (Oppenheimer *et al.*, 2011) and experimental work (Iacovino *et al.*, 2013). As discussed above, the natural phase assemblages of the starting lavas in this study could be approximated only under extremely H_2O-poor conditions. Even for KI-type lavas, which are slightly wetter than the AW lavas, our experiments suggest that low-H_2O conditions dominate ($X H_2 O^{fluid} \sim 0.2$). More evolved kaersutite-bearing lavas of the DVDP lineage were best reproduced in terms of modal abundance of amphibole ($<3–5\%$) only in experiments with higher H_2O contents (low-H_2O runs containing 15–19% amphibole), indicating a possible increase in water activity in evolved DVDP magmas. Given that the Erebus system is thought to be fluid-saturated, our results agree with the conclusions of Oppenheimer *et al.* (2011), who suggested that carbon-induced dehydration of Erebus magmas at various depths promotes crystal fractionation and magmatic differentiation.

Even though our driest experimental melts contain only 1–2 wt % H_2O, insufficient plagioclase crystallization and higher than observed CaO contents in our experimental glasses indicate that our experimentally established liquid line of descent is more water rich than the natural system. This suggests a maximum H_2O content of 1–2 wt % in Ross Island basanites and a maximum of $\sim$1 wt % in EL phonotephrites. Moussallam *et al.* (2013) demonstrated that evolved Erebus melts (i.e. lava lake phonolite) must have extremely low water contents, with a maximum of $\sim$0·5 wt % (but probably even below 0·2 wt %). The very tight constraints that these two studies place on the maximum water contents of Erebus magmas very closely match the trends in H_2O contents of Erebus melt inclusions (Oppenheimer *et al.*, 2011), which range from 1–2 wt % in basanite to $\leq$0·5 wt % in all other lavas, phonolites having $\leq$0·2 wt %.

Our results are consistent with the presence of a CO_2-rich fluid in the EL plumbing system but not in the DVDP. Given that both lineages are thought to be derived from the same parental melt (Kyle *et al.*, 1992), we suggest that a sustained connection of the EL plumbing system to its deep mantle source and a subsequent CO_2-rich fluid flux that characterizes the EL (and lack of such in the DVDP) is responsible for the differences in storage conditions and thus mineralogy of the two lava suites. The decoupled ascent of CO_2-rich vapor through the magmatic system of Erebus may explain the extreme dehydration of the EL melts, as CO_2 will degas early and deep and leach H_2O from the melt and into the vapor phase upon ascent (Métrich & Wallace, 2008). CO_2 fluxing through the EL system can also explain the sustained high-temperature regime of EL magmas inferred from phase equilibria (i.e. olivine–kaersutite stability) and would suggest a more reducing environment relative to the DVDP, consistent with enhanced kaersutite stability under oxidizing conditions.

One source, two lava lineages: pre-eruptive histories of EL and DVDP magmas

Based on our experimental results and the observations presented here, we propose two differentiation pathways from a single basanitic parent magma for the Ross Island lavas: a high-temperature pathway, followed by EL lavas, and a low-temperature pathway, followed by DVDP lavas. The parental magma beneath Erebus is a high-temperature ($>$1050°C) basanite that accumulated at high pressure, perhaps in the upper mantle (Kyle, 1981) or lower crust (Oppenheimer *et al.*, 2011). Both EL and DVDP basanites must have ascended rapidly (with little to no differentiation during ascent; Kyle, 1981), sourced directly from a high-temperature region near the crust–mantle boundary, as they both contain olivine phenocrysts. Rapid magma ascent is supported by the observation of mantle xenoliths within some basanites (see, e.g. Moore & Gullikson, 2013). The sustained high-temperature regime inferred for the EL ($>$1050°C) could be facilitated by the direct connection of the EL conduit to the hot parental magma storage region beneath Erebus. The sustained open-vent nature of Erebus volcano implies a continual resupply of heat and gas from a deep source region (Oppenheimer & Kyle, 2008; Oppenheimer *et al.*, 2009, 2011; Iacovino *et al.*, 2013a; Moussallam *et al.*, 2013). The difference in high- and low-temperature regimes, coupled with the fact that EL lavas have erupted continuously whereas DVDP lavas have stopped erupting, suggests that the DVDP plumbing system was a shorter-lived offshoot of the main Erebus conduit with little resupply of heat from the source region. This is consistent with the model proposed for the formation of the subsidiary Ross Island volcanic centers in which magma followed radial fractures created by the updoming of mantle material into the crust directly beneath Erebus (Kyle & Cole, 1974; Kyle *et al.*, 1992). More extensive dating of Hut Point Peninsula rocks would be necessary to precisely constrain the timing and longevity of the activity associated with DVDP lavas.

The DVDP magmas travelled along an offshoot of the main Erebus conduit, culminating at the surface on Hut Point Peninsula. During their rapid ascent, some olivine was removed from the DVDP basanites and injected into subsequently produced intermediate magmas as xenocrysts. Temperature decreased to below $\sim$1050°C during differentiation of the intermediate and evolved magmas, evidenced by the lack of olivine phenocrysts and the presence of kaersutite in all subsequent lava types. This drop in temperature may be

facilitated by the lack of continuous heat input from the source region coupled with long travel times through the shallow crust compared with the EL lavas.

CONCLUSIONS

Experiments were performed to constrain and compare the conditions of deep and intermediate magma storage and differentiation of EL and DVDP lavas. Our results indicate relatively dry conditions ($<$1–2 wt % H_2O) for both lineages, established by the plagioclase liquidus. The appearance of kaersutitic amphibole in natural intermediate and evolved DVDP lavas indicates an elevated water activity for the DVDP plumbing system compared with the EL, which does not contain kaersutite. The co-precipitation of kaersutite and plagioclase in natural DVDP lavas places very tight constraints on the H_2O content of the intermediate DVDP magmas, as phonotephrite experiments produce this assemblage only between XH_2O^{fluid} *c.* 0·15 and 0·35. Previous studies on kaersutite-bearing rocks have shown that kaersutite can be stabilized at such low water activities by the replacement of OH^- in the crystal structure by F^- and Cl^-, and via oxy-substitutions (see above). This, combined with the approximate reproduction of the natural phase assemblages in our experiments at $NNO + 1·5$ to $NNO + 2·0$, indicates that similarly oxidizing conditions may be present during deep and intermediate magma storage. We can also constrain temperature conditions for both lineages based on the presence or lack of olivine and kaersutite, for which our experiments indicate a peritectic-like relationship at intermediate melt water contents and $\sim$1050°C. Olivine is present in all EL lavas and in DVDP basanites, but is absent in intermediate and evolved DVDP rocks. The opposite is true of kaersutite, which appears only in intermediate and evolved DVDP rocks. Because kaersutite is stable to very low melt water contents (with its stability field increasing with evolution of the melt), we infer that the lack of kaersutite in EL lavas and DVDP basanites is the result of sustained high temperatures during deep and intermediate magmatic differentiation ($>$1050°C) and that kaersutite is stabilized in DVDP magmas owing to a drop in equilibration temperature from above 1050°C in basanites to below 1050°C in the intermediate magmas. The differences in T, XH_2O^{fluid}, and possibly fO_2 between DVDP and EL magmas can be explained by the EL plumbing system being dominated by the flux of a CO_2-rich fluid (as hypothesized in previous studies) and the lack of such a fluid in the DVDP. This is consistent with the model of the formation of Erebus and its subsidiary volcanic centers.

ACKNOWLEDGEMENTS

FUNDING

SUPPLEMENTARY DATA

Supplementary data for this paper are available at *Journal of Petrology* online.

REFERENCES

Allard, P. (2010). A CO_2-rich gas trigger of explosive paroxysms at Stromboli basaltic volcano, Italy. *Journal of Volcanology and Geothermal Research* **189**, 363–374.

Andújar, J., Costa, F. & Martí, J. (2010). Magma storage conditions of the last eruption of Teide volcano (Canary Islands, Spain). *Bulletin of Volcanology* **72**, 381–395.

Behrens, H., Misiti, V., Freda, C., Vetere, F., Botcharnikov, R. E. & Scarlato, P. (2009). Solubility of H_2O and CO_2 in ultrapotassic melts at 1200 and 1250–C and pressure from 50 to 500 MPa. *American Mineralogist* **94**, 105–120.

Burgisser, A. & Scaillet, B. (2007). Redox evolution of a degassing magma rising to the surface. *Nature* **445**, 194–197.

Burgisser, A., Oppenheimer, C., Alletti, M., Kyle, P. R., Scaillet, B. & Carroll, M. R. (2012). Backward tracking of gas chemistry measurements at Erebus volcano. *Geochemistry, Geophysics, Geosystems* **13**(**11**), doi:10.1029/2012GC004243.

Caldwell, D. A. & Kyle, P. R. (1994). Mineralogy and geochemistry of ejecta erupted from Mount Erebus, Antarctica, between 1972 and 1986. *Volcanological and environmental studies of Mount Erebus, Antarctica*, 147–162.

Carmichael, I. S. & Ghiorso, M. S. (1990). The effect of oxygen fugacity on the redox state of natural liquids and their crystallizing phases. In: Nicholls, J. & Russell, J. K. (eds) *Modern Methods of Igneous Petrology: Understanding Magmatic Processes. Mineralogical Society of America, Reviews in Mineralogy* **24**, 191–212.

Curtis, A. & Kyle, P. (2011). Geothermal point sources identified in a fumarolic ice cave on Erebus volcano, Antarctica using fiber optic distributed temperature sensing. *Geophysical Research Letters* **38**(**16**), L16802.

Cioni, R. (2000). Volatile content and degassing processes in the AD 79 magma chamber at Vesuvius (Italy). *Contributions to Mineralogy and Petrology* **140**, 40–54.

Cocheo, PA. (1993). *The solubility of water in basanitic melts at low pressures*, Masters thesis. Arizona State University.

Di Carlo, I., Pichavant, M., Rotolo, S. G. & Scaillet, B. (2006). Experimental crystallization of a high-K arc basalt: the golden pumice, Stromboli volcano (Italy). *Journal of Petrology* **47**, 1317–1343.

Di Carlo, I., Rotolo, S. G., Scaillet, B., Buccheri, V. & Pichavant, M. (2010). Phase equilibrium constraints on pre-eruptive conditions of recent felsic explosive volcanism at Pantelleria Island, Italy. *Journal of Petrology* **51**, 2245–2276.

Dixon, J. E. & Pan, V. (1995). Determination of the molar absorptivity of dissolved carbonate in basanitic glass. *American Mineralogist* **80**(11–12), 1339–1342.

Dixon, J. E., Stolper, E. M. & Holloway, J. R. (1994). An experimental study of water and carbon dioxide solubilities in mid-ocean ridge basaltic liquids. *Journal of Petrology* **36**, 1607–1631.

Dunbar, N. W., Cashman, K. V. & Dupré, R. (1994). Crystallization processes of anorthoclase phenocrysts in the Mount Erebus magmatic system: evidence from crystal composition, crystal size distributions, and volatile contents of melt inclusions. *Volcanological and environmental studies of Mount Erebus, Antarctica*, 129–146.

Feig, S. T., Koepke, J. & Snow, J. E. (2010). Effect of oxygen fugacity and water on phase equilibria of a hydrous tholeiitic basalt. *Contributions to Mineralogy and Petrology* **160**, 551–568.

Fine, G. & Stolper, E. (1986). Dissolved carbon dioxide in basaltic glasses: concentrations and speciation. *Earth and Planetary Science Letters* **76**, 263–278.

Flowers, G. C. (1979). Correction of Holloway's (1977) adaptation of the modified Redlich–Kwong equation of state for calculation of the fugacities of molecular species in supercritical fluids of geologic interest. *Contributions to Mineralogy and Petrology* **69**, 315–318.

Freise, M., Holtz, F., Koepke, J., Scoates, J. & Leyrit, H. (2003). Experimental constraints on the storage conditions of phonolites from the Kerguelen Archipelago. *Contributions to Mineralogy and Petrology* **145**, 659–672.

Harrison, T. M. & Watson, E. B. (1984). The behavior of apatite during crustal anatexis: equilibrium and kinetic considerations. *Geochimica et Cosmochimica Acta* **48**, 1467–1477.

Holloway, J. R. (1971). Internally heated pressure vessels. In: Ulmer, G.C. (ed) *Research Techniques for High Pressure and High Temperature*. Berlin, pp. 217–258.

Holloway, J. R. (1977). Fugacity and activity of molecular species in supercritical fluids. In: Fraser, D.G. (ed) *Thermodynamics in Geology*. Dordrecht, pp. 161–181.

Iacono-Marziano, G., Gaillard, F., Scaillet, B., Pichavant, M. & Chiodini, G. (2009). Role of non-mantle CO_2 in the dynamics of volcano degassing: The Mount Vesuvius example. *Geology* **37**, 319–322.

Iacovino, K., Moore, G., Roggensack, K., Oppenheimer, C. & Kyle, P. (2013). H_2O–CO_2 solubility in mafic alkaline magma: applications to volatile sources and degassing behavior at Erebus volcano, Antarctica. *Contributions to Mineralogy and Petrology* **166**, 845–860.

Ihinger, P. D., Hervig, R. L. & McMillan, P. F. (1994). Analytical methods for volatiles in glasses. In: Carroll, M. R. & Holloway, J. R. (eds) *Volatiles in Magmas. Mineralogical Society of America, Reviews in Mineralogy* **30**, 67–121.

Kaszuba, J. P. & Wendlandt, R. F. (2000). Effect of carbon dioxide on dehydration melting reactions and melt compositions in the lower crust and the origin of alkaline rocks. *Journal of Petrology* **41**, 363–386.

Kyle, P. R. (1977). Mineralogy and glass chemistry of recent volcanic ejecta from Mt Erebus, Ross Island, Antarctica. *New Zealand Journal of Geology and Geophysics* **20**, 1123–1146.

Kyle, P. R. (1981). Mineralogy and geochemistry of a basanite to phonolite sequence at Hut Point Peninsula, Antarctica, based on core from Dry Valley Drilling Project Drillholes 1, 2 and 3. *Journal of Petrology* **22**, 451–500.

Kyle, P. R. & Cole, J. W. (1974). Structural control of volcanism in the McMurdo Volcanic Group, Antarctica. *Bulletin Volcanologique* **38**, 16–25.

Kyle, P. R., Moore, J. A. & Thirlwall, M. F. (1992). Petrologic evolution of anorthoclase phonolite lavas at Mount Erebus, Ross Island, Antarctica. *Journal of Petrology* **33**, 849–875.

Lange, R. & Carmichael, I. (1987). Densities of Na_2O–K_2O–CaO–MgO–FeO–Fe_2O_3–Al_2O_3–TiO_2–SiO_2 liquids—New measurements and derived partial molar properties. *Geochimica et Cosmochimica Acta* **51**, 2931–2946.

Marianelli, P., Sbrana, A., Métrich, N. & Cecchetti, A. (2005). The deep feeding system of Vesuvius involved in recent violent strombolian eruptions. *Geophysical Research Letters* **32**(2). doi:10.1029/2004GL021667.

Martí, J., Andújar, J., Costa, F. & Wolff, J. (2008). Pre-eruptive conditions of the phonolitic magma from the El Abrigo caldera-forming eruption (Las Cañadas caldera, Tenerife, Canary Islands). In: *IOP Conference Series: Earth and Environmental Science*, doi:10.1088/1755-1307/3/1/012013.

Métrich, N. & Wallace, P. J. (2008). Volatile abundances in basaltic magmas and their degassing paths tracked by melt inclusions. In: Putirka, K. D. & Tepley, F. J., III (eds) *Minerals, Inclusions and Volcanic Processes. Mineralogical Society of America and Geochemical Society, Reviews in Mineralogy and Geochemistry* **69**, 363–402.

Molina, I., Burgisser, A. & Oppenheimer, C. (2012). Numerical simulations of convection in crystal-bearing magmas: A case study of the magmatic system at Erebus, Antarctica. *Journal of Geophysical Research: Solid Earth (1978–2012)* **117**(B7). doi:10.1029/2011JB008760.

Moore, G. & Carmichael, I. S. E. (1998). The hydrous phase equilibria (to 3 kbar) of an andesite and basaltic andesite from western Mexico: constraints on water content and conditions of phenocryst growth. *Contributions to Mineralogy and Petrology* **130**(3–4), 304–319.

Moore, G. & Gullikson, A. (2013). Crystal/liquid thermobarometry in the rapidly erupted Peridot Mesa phonotephrite: constraints from new measurements and phase equilibria experiments [abstract]. *AGU Fall Meeting Abstracts*, **1**(B1).

Morizet, Y., Brooker, R. A. & Kohn, S. C. (2002). CO_2 in haplophonolite melt: solubility, speciation and carbonate complexation. *Geochimica et Cosmochimica Acta* **66**, 1809–1820.

Moussallam, Y., Oppenheimer, C., Scaillet, B. & Kyle, P. R. (2013). Experimental phase-equilibrium constraints on the phonolite magmatic system of Erebus Volcano, Antarctica. *Journal of Petrology* **54**, 1285–1307.

Moussallam, Y., Oppenheimer, C., Scaillet, B., Gaillard, F., Kyle, P., Peters, N., & Donovan, A. (2014). Tracking the changing oxidation state of Erebus magmas, from mantle to surface, driven by magma ascent and degassing. *Earth and Planetary Science Letters* **393**, 200–209.

Nichols, A. R. L. & Wysoczanski, R. J. (2007). Using micro-FTIR spectroscopy to measure volatile contents in small and unexposed inclusions hosted in olivine crystals. *Chemical Geology* **242**, 371–384.

Ochs, F. A. & Lange, R. A. (1999). The density of hydrous magmatic liquids. *Science* **283**(5406), 1314–1317.

Oppenheimer, C. & Kyle, P. R. (2008). Probing the magma plumbing of Erebus volcano, Antarctica, by open-path FTIR

spectroscopy of gas emissions. *Journal of Volcanology and Geothermal Research* **177**, 743–754.

Oppenheimer, C., Lomakina, A. S., Kyle, P. R., Kingsbury, N. G. & Boichu, M. (2009). Pulsatory magma supply to a phonolite lava lake. *Earth and Planetary Science Letters* **284**, 392–398.

Oppenheimer, C., Moretti, R., Kyle, P. R., Eschenbacher, A., Lowenstern, J. B., Hervig, R. L. & Dunbar, N. W. (2011). Mantle to surface degassing of alkalic magmas at Erebus volcano, Antarctica. *Earth and Planetary Science Letters* **306**, 261–271.

Pandya, N., Muenow, D. W. & Sharma, S. K. (1992). The effect of bulk composition on the speciation of water in submarine volcanic glasses. *Geochimica et Cosmochimica Acta* **56**, 1875–1883.

Pichavant, M., Di Carlo, I., Le Gac, Y., Rotolo, S. G. & Scaillet, B. (2009). Experimental constraints on the deep magma feeding system at Stromboli volcano, Italy. *Journal of Petrology* **50**, 601–624.

Pichavant, M., Scaillet, B., Pommier, A., Iacono-Marziano, G. & Cioni, R. (2014). Nature and evolution of primitive Vesuvius magmas: an experimental study. *Journal of Petrology* **55**, 2281–2310.

Popp, R. K. & Phillips, M. W. (1995). An experimental study of phase equilibria and Fe oxy-component in kaersutitic amphibole; implications for the f_{H2} and α_{H2O} in the upper mantle. *American Mineralogist* **80**, 534–548.

Popp, R. K. & Taras Bryndzia, L. (1992). Statistical analysis of Fe^{3+}, Ti, and OH in kaersutite from alkalic igneous rocks and mafic mantle xenoliths. *American Mineralogist* **77**, 1250–1250.

Prouteau, G. & Scaillet B. (2003). Experimental constraints on the origin of the 1991 Pinatubo dacite. *Journal of Petrology* **44**, 2203–2241.

Robie, R. A. & Hemingway, B. S. (1979). *Thermodynamic properties of minerals and related substances at 298.15 K and 1 bar (105 pascals) pressure and at higher temperatures (No. 2131).* USGPO; For sale by US Geological Survey, Information Services.

Roux, J. & Lefevre, A. (1992). A fast-quench device for internally heated pressure vessels. *European Journal of Mineralogy* **4**, 279–281.

Sack, R. O., Walker, D. & Carmichael, I. S. (1987). Experimental petrology of alkalic lavas: constraints on cotectics of multiple saturation in natural basic liquids. *Contributions to Mineralogy and Petrology* **96**, 1–23.

Scaillet, B., Pichavant, M., Roux, J., Humbert, G. & Lefevre, A. (1992). Improvements of the Shaw membrane technique for measurement and control of fH$_2$ at high temperatures and pressures. *American Mineralogist* **77**, 647–655.

Shaw, H. R. & Wones, D. R. (1964). Fugacity coefficients for hydrogen gas between 0 degrees and 1000 degrees C, for pressures to 3000 atm. *American Journal of Science* **262**, 918–929.

Shinohara, H., Aiuppa, A., Giudice, G., Gurrieri, S. & Liuzzo, M. (2008). Variation of H_2O/CO_2 and CO_2/SO_2 ratios of volcanic gases discharged by continuous degassing of Mount Etna volcano, Italy. *Journal of Geophysical Research: Solid Earth (1978–2012)* **113**(**B9**), 1978–2012.

Spera, F. J. (1984). Carbon dioxide in petrogenesis III: role of volatiles in the ascent of alkaline magma with special reference to xenolith-bearing mafic lavas. *Contributions to Mineralogy and Petrology* **88**, 217–232.

Spilliaert, N., Allard, P., Métrich, N. & Sobolev, A. V. (2006). Melt inclusion record of the conditions of ascent, degassing, and extrusion of volatile-rich alkali basalt during the powerful 2002 flank eruption of Mount Etna (Italy). *Journal of Geophysical Research: Solid Earth (1978–2012)* **111**(**B4**), doi:10.1029/2005JB003934.

Sun, S. S. & Hanson, G. N. (1975). Origin of Ross Island basanitoids and limitations upon the heterogeneity of mantle sources for alkali basalts and nephelinites. *Contributions to Mineralogy and Petrology* **52**, 77–106.

Sun, S. S. & Hanson, G. N. (1976). Rare earth element evidence for differentiation of McMurdo volcanics, Ross Island, Antarctica. *Contributions to Mineralogy and Petrology* **54**, 139–155.

Tagliani, S. M., Nicotra, E., Viccaro, M. & Gianfagna, A. (2012). Halogen-dominant mineralization at Mt. Calvario dome (Mt. Etna) as a response of volatile flushing into the magma plumbing system. *Mineralogy and Petrology* **106**(**1–2**), 89–105.

Walker, J. A., Roggensack, K., Patino, L. C., Cameron, B. I. & Matías, O. (2003). The water and trace element contents of melt inclusions across an active subduction zone. *Contributions to Mineralogy and Petrology* **146**, 62–77.

Zandomeneghi, D., Aster, R., Kyle, P., Barclay, A., Chaput, J. & Knox, H. (2013). Internal structure of Erebus volcano, Antarctica imaged by high-resolution active-source seismic tomography and coda interferometry. *Journal of Geophysical Research: Solid Earth* **118**, 1067–1078.